Monthly Notices of the ROYAL ASTRONOMICAL SOCIETY

MNRAS **546,** 1–19 (2026) https://doi.org/10.1093/mnras/stag119
Advance Access publication 2026 January 19

The dark side of early galaxies: GEKO uncovers dark-matter fractions at $z \sim 4-6$

A. Lola Danhaive [1,2★] Sandro Tacchella [1,2] Andrew J. Bunker [3] Emma Curtis-Lake [4] Anna de Graaff [5] Francesco D'Eugenio [1,2] Qiao Duan [1,2] Eiichi Egami [6] Daniel J. Eisenstein [7] Benjamin D. Johnson [7] Roberto Maiolino [1,2] William McClymont [1,2] Marcia Rieke [6] Brant Robertson [8] Fengwu Sun [7] Christopher N. A. Willmer [6] Zihao Wu [7] and Yongda Zhu [6]

[1]*Kavli Institute for Cosmology, University of Cambridge, Madingley Road, Cambridge CB3 0HA, UK*
[2]*Cavendish Laboratory, University of Cambridge, 19 JJ Thomson Avenue, Cambridge CB3 0HE, UK*
[3]*Department of Physics, University of Oxford, Denys Wilkinson Building, Keble Road, Oxford OX1 3RH, UK*
[4]*Centre for Astrophysics Research, Department of Physics, Astronomy and Mathematics, University of Hertfordshire, Hatfield AL10 9AB, UK*
[5]*Max-Planck-Institut für Astronomie, Königstuhl 17, D-69117 Heidelberg, Germany*
[6]*Steward Observatory, University of Arizona, 933 N. Cherry Avenue, Tucson, AZ 85721, USA*
[7]*Center for Astrophysics | Harvard & Smithsonian, 60 Garden St, Cambridge, MA 02138,USA*
[8]*Department of Astronomy and Astrophysics, University of California, Santa Cruz, 1156 High Street, Santa Cruz, CA 95064, USA*

Accepted 2026 January 13. Received 2025 December 28; in original form 2025 November 23

ABSTRACT

James Webb Space Telescope (*JWST*)/NIRCam slitless spectroscopy enables dynamical mass measurements for typical star-forming galaxies only a billion years after the big bang. We model the Hα morpho-kinematics of 163 galaxies at redshift $z \approx 4$–6 from FRESCO and CONGRESS (with JADES imaging), using the GEKO code, and infer rotational velocities and dispersions within r_e. Our sample spans $\log M_\star \approx 7$–10 and $\log M_{dyn} \approx 9$–11. Gas masses are inferred from empirical scaling relations and combined with stellar masses to yield baryonic masses. The resulting median inferred gas-to-baryonic mass fraction is $\langle f_{gas} \rangle = 0.77$. Using these baryonic masses together with the dynamical masses, we derive dark-matter fractions $f_{DM}(r < r_e)$ within the Hα half-light radius, and find a high median value of $\langle f_{DM} \rangle = 0.73$, where f_{DM} is defined relative to the total (DM + baryonic) mass. About two-thirds of systems are DM-dominated within $r_e \sim 0.5$–1 kpc. We find that f_{DM} decreases with stellar mass, consistent with predictions from simulations. The stellar Tully–Fisher relation shows a tentative offset to higher v_{circ} at fixed $M_\star$ and substantial intrinsic scatter, suggesting that the relation is only beginning to emerge at $z \sim 5$. We measure a negative correlation between f_{DM} and baryonic surface density Σ_{bar}, weaker but broadly consistent with trends at cosmic noon and at $z \sim 0$. Qualitatively comparing with modified NFW profiles coupled to an empirical stellar-to-halo mass relation suggests that the lowest f_{DM} ($\lesssim 0.4$) require cored inner DM profiles, while the highest fractions favour cuspier profiles, potentially reflecting adiabatic contraction. Overall, the elevated f_{gas} and f_{DM} at $z \gtrsim 4$ are compatible with progenitors of baryon-dominated systems at $z \sim 2$ and naturally anticipate overmassive black holes at fixed $M_\star$.

Key words: galaxies: evolution – galaxies: high-redshift – galaxies: kinematics and dynamics – galaxies: structure – dark matter.

1 INTRODUCTION

The nature and physics of dark matter (DM) is, to this day one of the biggest outstanding questions in astrophysics. In the widely adopted standard cosmological model of Lambda cold dark matter (ΛCDM), DM haloes form from the collapse of overdensities in the early Universe, allowing baryons to accrete, cool, and form stars. This process is the basis of galaxy formation and predicts the hierarchical growth of galaxies. However, the physics and interplay between the baryons and the DM remain remarkably poorly constrained.

In fact, measuring the DM mass content of galaxies and their haloes observationally is a challenge, as often even the full baryonic mass is difficult to constrain. Many approaches have been adopted to indirectly constrain the galaxy–halo connection, such as abundance matching (C. Marinoni & M. J. Hudson 2002; A. V. Kravtsov et al. 2004; C. Conroy, R. H. Wechsler & A. V. Kravtsov 2006; A. Vale & J. P. Ostriker 2006; A. Tasitsiomi 2007) and clustering analyses (J. A. Peacock & R. E. Smith 2000; A.

★ E-mail: ald66@cam.ac.uk

Cooray & R. Sheth 2002; R. E. Smith et al. 2003; L. Paquereau et al. 2025) based on *N*-body simulations. Many numerical simulations have measured the stellar-to-halo mass (SMHM) relation and its evolution with redshift (P. S. Behroozi, C. Conroy & R. H. Wechsler 2010; B. P. Moster et al. 2010; A. Rodríguez-Puebla et al. 2017; S. Tacchella et al. 2018; P. Behroozi et al. 2019), although its overall normalization and turnover mass are still debated and model-dependent. In part, this is due to the circularity of modelling inputs and outputs, as cosmological hydrodynamical simulations are usually calibrated to SMHM relations measured from abundance matching or derived from semi-empirical models. Placing direct observational constraints on this relation would offer important insight on the integrated strength of various fundamental mechanisms that govern the evolution of galaxies, such as stellar feedback, black hole activity, and mergers.

One of the most robust ways of constraining the DM content within galaxies is through the measurement of galaxy kinematics. The rotation curves and pressure support of galaxies reflect their total density profile, providing an estimate of the DM content assuming that the baryonic content is known and that the galaxies are at equilibrium (V. C. Rubin, W. K. Ford & N. Thonnard 1980; A. Burkert 1995; M. Persic, P. Salucci & F. Stel 1996; A. Burkert & J. Silk 1997; P. J. McMillan 2017; Y. Zhu et al. 2023). The fraction of DM to the total mass, $f_{\rm DM}$, is a by-product of the mass assembly history of galaxies and of their current growth (see R. H. Wechsler & J. L. Tinker 2018, and references therein).

The study of these density profiles within dwarf galaxies, defined as having masses of $M_\star < 3 \times 10^9\,{\rm M}_\odot$, has proved particularly fruitful, revealing a discrepancy between ΛCDM-predicted and observed density profiles known as the core–cusp problem. Where collisionless (cold) DM-only cosmological simulations predict cuspy profiles, with densities increasing steeply at small radii, measurements of the rotation curves in dwarf galaxies in the local Universe show 'core'-like profiles that flatten at central radii (B. Moore 1994; A. Burkert 1995; W. J. G. Blok 2010; J. S. Bullock & M. Boylan-Kolchin 2017). This core–cusp problem posed a direct challenge to ΛCDM, with propositions of different types of DM surfacing (W. Hu, R. Barkana & A. Gruzinov 2000; D. N. Spergel & P. J. Steinhardt 2000). However, many studies have now shown that this problem can be alleviated by invoking strong baryonic feedback, likely from supernovae. This feedback, especially through repeated bursts of star formation, can flatten the DM cusp into a core (J. I. Read & G. Gilmore 2005; A. Pontzen & F. Governato 2012, 2014; D. Martizzi, R. Teyssier & B. Moore 2013; A. A. El-Zant, J. Freundlich & F. Combes 2016; J. Freundlich et al. 2020a; A. Dekel et al. 2021; Z. Li et al. 2023). This process has been observed in hydrodynamical simulations (e.g. T. K. Chan et al. 2015; J. I. Read, O. Agertz & M. L. M. Collins 2016, and references therein), but details such as mass, redshift, and environmental dependence remain uncertain. Interestingly, cases of profiles cuspier than ΛCDM profiles have also been found (A. Sonnenfeld et al. 2012; Y. Wang et al. 2020; P. Li et al. 2022), which could be caused by adiabatic contraction of the DM halo due to high baryonic densities in the galaxy core (G. R. Blumenthal et al. 1986; O. Y. Gnedin et al. 2004; A. Di Cintio et al. 2014; E. Tollet et al. 2016; P. Li et al. 2022).

Another important relation that relates the potential of the DM halo to its host galaxy is the observed tight relation between stellar (or baryonic) mass and circular velocity, named the stellar (or baryonic) Tully–Fisher relation (TFR; R. B. Tully & J. R. Fisher 1977). The baryonic mass TFR (bTFR) is the more fundamental of the two, as it holds even down to low masses (S. S. McGaugh et al. 2000; S. S. McGaugh 2005). Both TFRs have been found to hold for star-forming galaxies from $z \approx 0-1$ (R. Reyes et al. 2011; F. Lelli, S. S. McGaugh & J. M. Schombert 2016) to cosmic noon (S. H. Miller et al. 2011; H. Übler et al. 2017), albeit with an increase of scatter and a decrease of zero-point offset with redshift. Measuring the position of galaxies on the TFR plane at $z > 4$ can provide constraints on the properties of the underlying haloes and their relative contribution to the total mass of the galaxy.

The detailed mapping of rotation curves of galaxies in the local Universe has revealed that $\log(M_\star[{\rm M}_\odot]) = 10-11$ star-forming galaxies are baryon-dominated in their central ∼1 kpc, but DM-dominated within their half-light, or effective, radii $r_{\rm e}$ (V. C. Rubin et al. 1985; T. P. K. Martinsson et al. 2013). On the other hand, early-type galaxies (ETGs) at $z \sim 0$ are heavily baryon-dominated within $r_{\rm e}$, suggesting a diverging mass assembly history (E. Noordermeer et al. 2007; M. Cappellari et al. 2013a; P. Serra et al. 2016). At $z \sim 1$, B. I. Ciocan et al. (2025) probed galaxies down to low stellar masses ($\log(M_\star[{\rm M}_\odot]) = 7-11$) and found they remain predominantly DM-dominated (see also N. F. Bouché et al. 2022). Interestingly, studies of DM fractions at cosmic noon ($z \approx 2$) in $\log(M_\star[{\rm M}_\odot]) \gtrapprox 9.5$ galaxies found them to be similar to local ETGs, which are typically baryon-dominated in their central regions (S. H. Price et al. 2016; S. Wuyts et al. 2016; R. Genzel et al. 2017, 2020; A. Nestor Shachar et al. 2023). R. Genzel et al. (2020) interpret these findings as evidence for cored DM profiles in these cosmic noon galaxies, motivated by the rapid formation of massive haloes and galaxies at $z \sim 1-3$. In fact, cosmic noon marks the peak of the cosmic star formation rate (SFR) density (P. Madau & M. Dickinson 2014), where gas accretion rates reached peak values (L. J. Tacconi, R. Genzel & A. Sternberg 2020) and stellar mass doubling scales were on the order of $t < 0.4$Gyr.

Measurement of the DM content of high-redshift galaxies ($z \geq 4$) was made possible with the advent of the *James Webb Space Telescope* (*JWST*), whose Near-Infrared Camera (NIRCam) and Near-Infrared Spectrograph (NIRSpec) instruments probe ionized gas emission lines out to $z \sim 10$. While kinematic studies had previously been done at such early times through cold gas measurements (i.e. [C II] or CO) from ground-based telescopes such as the Atacama Large Millimeter Array (ALMA; e.g. F. Rizzo et al. 2020, 2021; F. Lelli et al. 2021; A. Pope et al. 2023; F. Roman-Oliveira, F. Fraternali & F. Rizzo 2023; L. E. Rowland et al. 2024), the lack of constraints on the stellar mass made estimating $f_{\rm DM}$ difficult. Using kinematic modelling of *JWST*/NIRSpec Multi Shutter Array (MSA) data (see also A. Saldana-Lopez et al. 2025), A. de Graaff et al. (2024a) and A. de Graaff, A. Pillepich & H.-W. Rix (2024b) found that the five low-mass $\log(M_\star[{\rm M}_\odot]) < 9$ galaxies in their $z \sim 6-8$ sample were DM dominated within $r_{\rm e}$ ($f_{\rm DM} \sim 0.7$). By studying similar galaxies in the TNG50 simulations (A. Pillepich et al. 2019), A. de Graaff et al. (2024b) suggest that DM-dominated $\log(M_\star[{\rm M}_\odot]) = 8-9$ galaxies at $z \sim 6$ are the progenitors of massive baryon-dominated systems at $z \sim 2$. This finding predicts a DM dominated phase of early galaxy formation, with expectations that all low-mass galaxies have low baryon fractions in their central region.

When studying the DM fractions in the central regions of galaxies, it is also important to consider the effects of black holes (BHs), which could be hosted in their cores. Although BHs have been shown to have masses which are only a small fraction of the total dynamical mass (J. Kormendy & L. C. Ho 2013), recent *JWST*

studies have uncovered 'overmassive' BHs in the early Universe, with $M_{\rm BH}/M_\star \sim 0.1 - 0.01$ (Y. Harikane et al. 2023; V. Kokorev et al. 2023; H. Übler et al. 2023; R. Maiolino et al. 2024b; B. L. Jones et al. 2025; I. Juodžbalis et al. 2025a), even reaching $M_{\rm BH}/M_\star > 2$ (I. Juodžbalis et al. 2025b). If the relatively low-mass galaxies at $z > 4$ host massive black holes that experience accretion phases, then they could play a significant role in the galaxy's mass assembly history. Importantly, active galactic nuclei (AGNs)-driven outflows can heavily disrupt the surrounding gas, particularly in low-mass galaxies (D. Sijacki et al. 2007; D. Nelson et al. 2019; S. Koudmani, N. A. Henden & D. Sijacki 2021; S. Koudmani, D. Sijacki & M. C. Smith 2022; S. Carniani et al. 2024). The presence of such AGNs is important to study as it currently introduces more uncertainties in the interpretation of our kinematic measurements.

With the synergy of NIRCam imaging and grism data, the kinematics of ~ 200 galaxies at $z = 4 - 6$ were measured in A. L. Danhaive et al. (2025b) using a new forward-modelling Bayesian code, the Grism Emission-line Kinematics tOol (GEKO; A. L. Danhaive & S. Tacchella 2025)[1]. This sample is comprised of $\log(M_\star[\rm M_\odot]) \approx 7 - 10.5$ star-forming galaxies, with a wide range of rotational support v/σ_0. As shown in A. L. Danhaive et al. (2025b), many of these galaxies have large dynamical masses compared to their stellar masses, pointing to large contributions from gas and DM. In this paper, we study the mass content of these galaxies in detail, placing the first statistical constraints on DM fractions at high redshift $z > 4$. We briefly introduce our sample and methodology in Section 2, then present our dynamical mass measurements and discuss them in the context of the TFR relation in Section 3. We present our gas and DM fractions in Section 4, and compare them to samples at lower redshift. In Section 5, we interpret our measurements in the context of the shapes of DM density profiles, and explore potential contributions from BHs. Finally, we summarize our results in Section 6. Throughout this work, we assume $\Omega_0 = 0.315$ and $H_0 = 67.4\,\rm km\,s^{-1}\,Mpc^{-1}$ (Planck Collaboration VI 2020).

2 OBSERVATIONS, SAMPLE, AND METHODOLOGY

In this section, we present the NIRCam grism and imaging data used in this work, along with a description of our sample (Section 2.1). We also describe the morpho-kinematic modelling of our sample (Section 2.2), which is used to measure the rotational velocities and velocity dispersions of our galaxies. This sample, and the associated kinematic measurements, are described in A. L. Danhaive et al. (2025b), so we only summarize them here but refer the reader to that work for more details. Finally, in Section 2.3, we detail our derivation of the gas and DM fractions for our sample.

2.1 NIRCam data and sample selection

The analysis in this work uses both NIRCam imaging and grism spectroscopy. The NIRCam grism data are obtained from the FRESCO survey (PI: Oesch, PID: 1895; P. A. Oesch et al. 2023; A. Covelo-Paz et al. 2025) in the Great Observatories Origins Deep Survey - South (GOODS-S) and North (GOODS-N), and the CONGRESS survey (PIs: Egami & Sun, PID: 3577; Sun et al. in preparation) in GOODS-N. These surveys are comprised of grism data (R mode) in the $F444W$ and $F356W$ filters, respectively, probing Hα emission at $z = 3.8 - 6.5$. The data are reduced following F. Sun et al. (2023) and J. M. Helton et al. (2024) to obtain 2D spectra for each galaxy in the field of view. The 2D spectra are then continuum subtracted following the two-step iterative technique described in D. Kashino et al. (2023) to obtain 2D emission line maps for Hα.

In the regions of the FRESCO and CONGRESS surveys, there is a wealth of deep imaging data from the *JWST* Advanced Deep Extragalactic Survey (JADES) (D. J. Eisenstein et al. 2023; M. J. Rieke et al. 2023). Specifically, the JADES survey has imaging in most of the NIRCam wide bands, as well as the $F335M$ and $F410M$ medium bands. In addition, the FRESCO survey obtained imaging in the $F182M$ and $F210M$ bands, and CONGRESS in $F090W$ and $F115W$, complementing the existing JADES imaging data. For certain regions in our sample, we also have additional medium bands $F182M$, $F210M$, $F430M$, $F460M$, and $F480M$ from the *JWST* Extragalactic Medium Band Survey (JEMS; C. C. Williams et al. 2023) in GOODS-S. The full details on the data reduction and generation of the drizzled mosaics and photometric catalogues can be found in M. J. Rieke et al. (2023) and B. Robertson et al. (2024). This large array of photometric bands, in addition to the grism spectroscopic redshifts and emission line fluxes, allows us to fit the SEDs of all galaxies with PROSPECTOR (B. D. Johnson et al. 2021; S. Tacchella et al. 2023; C. Simmonds et al. 2024, 2025). We obtain measurements of the stellar masses ($M_\star$), SFRs, and star formation histories (SFHs) used in this work.

As mentioned above, the parent sample used in this work is described in A. L. Danhaive et al. (2025b). This Hα emitter sample is built on the photometric redshift estimates from EAZY (G. B. Brammer, P. G. van Dokkum & P. Coppi 2008; K. N. Hainline et al. 2024), which are then confirmed by Gaussian fitting of the 1D grism spectrum followed by visual inspection (J. M. Helton et al. 2024; X. Lin et al. 2025). We select galaxies with an Hα signal-to-noise (S/N) cut of 10 (582 galaxies), from which we select our final sample of 213 galaxies based on additional S/N cuts and position angle (PA) cuts to ensure that galaxies are at an angle with respect to the grism dispersion direction. Specifically, the 213 galaxies are separated into three samples based on the robustness of the kinematic measurements, as described in A. L. Danhaive et al. (2025b). In this paper, we only consider the 163 galaxies from the gold and silver samples, and we exclude the unresolved sample. The latter contains systems with sizes smaller than the full width half-maximum (FWHM) of the $F444W$ (or $F356W$) point spread function (PSF), or with unresolved velocity gradients. However, for simplicity, we do not further distinguish between the gold and silver sub-samples in this paper, treating the 163 galaxies together as our full final sample.

2.2 Morpho-kinematic modelling

To obtain measurements of the rotational velocity and velocity dispersion, we use the Bayesian-inference fitting tool GEKO (A. L. Danhaive & S. Tacchella 2025), which forward models the grism data and compares it with the observed 2D spectrum to obtain the posterior distributions of the input morphological and kinematic model parameters.

[1] Available at https://github.com/angelicalola-danhaive/geko.

The Hα emission line map is modelled with a Sérsic profile (J. L. Sersic 1968)

$$I(r) = I_e \exp\left(-b_n\left[\left(\frac{r}{r_e}\right)^{1/n} - 1\right]\right), \quad (1)$$

where I_e is the intensity at the effective radius r_e and n is the Sérsic index. We use the near-ultraviolet (UV) image from JADES, probed by the $F150W$ filter at $\lambda_{rest} \approx 2000$Å, as a prior for the morphology of the Hα line. The rest-frame near-UV is chosen because it traces young stars responsible for ionizing the nearby gas and producing the Hα emission. To model the $F150W$ images, we use the Bayesian code PYSERSIC (I. Pasha & T. B. Miller 2023), which models the image with a PSF-convolved Sérsic profile. The width of the priors is obtained by doubling the uncertainties obtained from the PYSERSIC modelling.

The Hα gas kinematics are modelled with an arctangent velocity curve (S. Courteau 1997; S. H. Miller et al. 2011)

$$V_{rot}(r_{int}, r_t, V_a) = \frac{2}{\pi} V_a \arctan\frac{r_{int}}{r_t}, \quad (2)$$

where V_{rot} is the rotational velocity at a given radius r_{int} in the intrinsic galaxy plane, V_a is the asymptotic value to which the arctangent rotation curve converges to at large radii $r_{int} \to \infty$, and r_t is the turn-around radius of the rotation curve. To project this velocity on the observation plane, we need to account for the galaxy's inclination i:

$$V_{obs}(x, y) = V_{rot}(r_{int}, r_t, V_a)\ \sin i\ \cos\phi_{int}, \quad (3)$$

where ϕ_{int} is the polar angle coordinate in the galaxy plane. To compute the inclination, we assume an intrinsic axis ratio $q_0 = 0.2$ to account for the thickness of galaxies at high redshift (S. Wuyts et al. 2016; R. Genzel et al. 2017; S. H. Price et al. 2020; H. Übler et al. 2024). We model the velocity dispersion as being constant across the galaxy, $\sigma_0(x, y) \equiv \sigma_0$.

The model Hα intrinsic map is convolved with the kinematics to form a model 3D cube, which is then convolved with the instrument PSF and line spread function (LSF). We approximate the PSF using the model PSFs (mPSFs) from Z. Ji et al. (2024) constructed by mosaicing WEBBPSF models repeatedly over the field identically to our JADES exposure mosaics and then measuring the average PSF. The model PSFs are then resampled down to the grism spatial pixelization. The wavelength-dependent 1D LSF is modelled as the sum of two Gaussian distributions to account for the broader wings. It was calibrated using SMP-LMC-058, a compact planetary nebula in the Large Magellanic Cloud (LMC; see also O. C. Jones et al. 2023) using extraction from *JWST* commissioning, Cycle-1 and 2 calibration observations (Sun et al. in preparation).

Finally, using the grism dispersion function, the cube is projected onto the observed grism 2D space. The priors for the kinematic parameters are uniform. We place a constraint on the turn-around radius r_t to be smaller than the effective radius r_e (S. H. Miller et al. 2011).

2.3 Gas and DM fractions

In order to infer gas masses from our SFRs, we use the empirical relations calibrated in L. J. Tacconi et al. (2020). We assume here that the gas component is dominated by the molecular phase, whose mass is constrained in these relations. In dense, highly star-forming systems, it is expected that the molecular phase dominates within r_e, and the atomic phase only contributes to a minor degree (e.g. A. K. Leroy et al. 2008; A. Saintonge et al. 2017). The ionized component is small in most systems (e.g. see R. C. Kennicutt & N. J. Evans 2012, and references therein). Given the small sizes ($r_e \approx 0.5 - 1$ kpc; A. L. Danhaive et al. 2025a) and high specific SFRs (sSFR, with mass-doubling time-scales of $t_{double} \lessapprox 30$ Myr) of the galaxies in our sample, this is a valid assumption.

In these equations, the molecular gas mass is estimated using the sSFR of the system and the integrated depletion time-scale for converting the gas into stars. This time-scale depends on the redshift and therefore provides a more accurate conversion than fixed redshift relations (e.g. J. Kennicutt 1998). Furthermore, the latter is calibrated to the local universe, where gas fractions are overall lower, whereas the L. J. Tacconi et al. (2020) relations are calibrated from $z \sim 0 - 5.5$ from almost 2000 objects or stacks (see also A. Saintonge et al. 2017; L. J. Tacconi et al. 2018; J. Freundlich et al. 2019). Specifically, the gas-to-stellar mass ratio $\mu_{gas} = M_{gas}/M_\star$ scales with redshift z, sSFRs, and stellar mass $M_\star$, where the scaling factors are computed using observational measurements of ionized and molecular gas from the literature. The relation for μ_{gas} is

$$\begin{aligned}\log\mu_{gas} &= A + B \times (\log(1+z) - F)^2 \\ &+ C \times \log(\mathrm{sSFR}/\mathrm{sSFR}_{MS}(z, M_\star)) \\ &+ D \times (\log M_\star - 10.7),\end{aligned}$$

with the SFMS defined as in J. S. Speagle et al. (2014), and the parameters A, B, C, D, and F are the parameters obtained in L. J. Tacconi et al. 2020 (table 2b) from error-weighed, multiparameter regression. SFMSs such as J. S. Speagle et al. (2014) can suffer from sample selection effects, especially on the low mass end, which can bias the inferred relation (e.g. W. McClymont et al. 2025b; C. Simmonds et al. 2025). None the less, we adopt the J. S. Speagle et al. (2014) SFMS when computing our gas fractions to stay consistent with how the scaling relations were calibrated. We also note that the J. Kennicutt (1998) relation assumes solar metallicities, which can have significant impacts (~ 0.3 dex) on the inferred SFRs, particularly for low-mass, metal-poor galaxies.

Using the aforementioned scaling relation, we can then calculate gas fractions on the galaxy scale,

$$f_{gas} = \frac{\mu_{gas}}{1 + \mu_{gas}} = \frac{M_{gas}}{M_{gas} + M_\star}, \quad (4)$$

and infer the total baryonic masses

$$M_{bar} = M_{gas} + M_\star = (\mu_{gas} + 1)M_\star. \quad (5)$$

To quantify the uncertainties in our inferred gas fractions, we propagate the uncertainties from the inputs to the scaling relation ($M_\star$ and SFR), along with the uncertainties of the constant parameters of the relation itself (A, B, C, D, and F). To assess the systematics introduced by our choice of gas mass estimate, we compare the f_{gas} measurements obtained from the scaling relation to those inferred by a simple conversion

$$M_{gas} = \mathrm{SFR} \times t_{dep} \quad (6)$$

with a depletion time $t_{dep} = 0.5 - 1$ Gyr. Although using this relation increases the intrinsic scatter, our median fractions remain consistent. If instead we change the SFMS used in the L. J. Tacconi et al. (2020) relation, from J. S. Speagle et al. (2014), and adopt the one from C. Simmonds et al. (2025), we find that our inferred gas fractions are on average higher by $\Delta f_{gas} \approx 0.05 - 0.1$.

We note that in both of these cases, the change in $f_{\rm gas}$ does not visibly affect the median values of our inferred dark-matter fractions. However, it is important to note these uncertainties in the gas fractions, which can only be addressed with constraints from direct observations of the molecular gas content.

In virial equilibrium, the circular velocity of galaxies at a radius r can be related to the combined effects of gravity and turbulence-induced pressure. The former is reflected in the rotational velocity, and the latter is an asymmetric drift correction to account for the pressure support (A. Burkert et al. 2010; S. F. Newman et al. 2013; S. Wuyts et al. 2016). For an exponential disc, the circular velocity can be written as

$$v_{\rm circ}(r) = \sqrt{v^2_{\rm rot}(r) + 2(r/r_{\rm s})\sigma_0^2}. \quad (7)$$

The above prescription for the asymmetric drift correction is derived in A. Burkert et al. (2010) assuming a constant dispersion profile and a vertical hydrostatic equilibrium in the disc. However, as discussed in N. F. Bouché et al. (2022), different assumptions can be made, such as assuming a constant disc thickness (J. J. Dalcanton & A. M. Stilp 2010), assuming a radially declining dispersion profile (L. Posti et al. 2018), or using a general thin disc approximation based on the Jeans equations (A.-M. Weijmans et al. 2008). Amongst these prescriptions, the A. Burkert et al. (2010) correction is the strongest, but typically strong deviations between these assumptions occur beyond $r = r_e$. Choosing a different prescription would lower our dynamical mass measurements and therefore lower the inferred DM fractions. The circular velocity reflects the gravitational potential of the galaxy and is hence directly related to the dynamical mass,

$$M_{\rm dyn} = k_{\rm tot}\frac{r_{\rm e}v^2_{\rm circ}(r_{\rm e})}{G}, \quad (8)$$

where G is the gravitational constant and $k_{\rm tot}$ is the virial coefficient (S. H. Price et al. 2020). The virial coefficient $k_{\rm tot}$ allows us to infer the total dynamical masses based on measurements out to $r_{\rm e}$. If we instead compute $v_{\rm circ}$ using a generalised Sérsic profile (rather than an exponential disc, $n = 1$), our inferred dynamical masses remain consistent within $\Delta(\log M_{\rm dyn}) \lesssim 0.07$ [with median $\Delta(\log M_{\rm dyn}) \lesssim 0.02$]. We present results for the exponential disc assumption to provide a more direct comparison to other works in the literature. Because we have modelled our galaxies with $q_0 = 0.2$, we choose $k_{\rm tot} = 1.8$ as it is the coefficient for galaxies with $q_0 = 0.2$ and $n \sim 1-4$ (S. H. Price et al. 2022). This coefficient is computed assuming the light distribution follows a Sérsic profile, a constant mass-to-light ratio, and an axisymmetric mass distribution. We note that varying q_0 in the interval $q_0 = 0.15 - 0.25$ shifts $\sin i$ by $\Delta(\sin i) \lesssim 0.05$, propagating to $\Delta(\log M_{\rm dyn}) \lesssim 0.05$. For more extreme values $q_0 = 0.50$, this correction can reach $\Delta(\log M_{\rm dyn}) \approx 0.1$.

Finally, using our dynamical mass measurements, we can compute the DM fractions

$$f_{\rm DM} = \frac{M_{\rm DM}}{M_{\rm dyn}} = \frac{M_{\rm dyn} - M_{\rm bar}}{M_{\rm dyn}}. \quad (9)$$

All our inferred fractions are calculated within the effective radius $r_{\rm e}$ since that is where our kinematic measurements are best constrained. We find that 20 per cent of our sample has negative and, therefore, unphysical DM fractions. This fraction drops to 18 per cent (8 per cent) when a deviation from $f_{\rm DM} = 0$ is required at the level of σ (3σ). These numbers are comparable to those reported in other studies (e.g. S. Wuyts et al. 2016), and suggest inconsistencies in the modelling of the SEDs and the kinematics, including for instance positive age gradients (C. D'Eugenio et al. 2021; J. Houdt et al. 2021) or non-equilibrium configurations. Although we discuss these systems in the text, unless otherwise mentioned we only consider systems with $f_{\rm DM} > 0$ for our analyses.

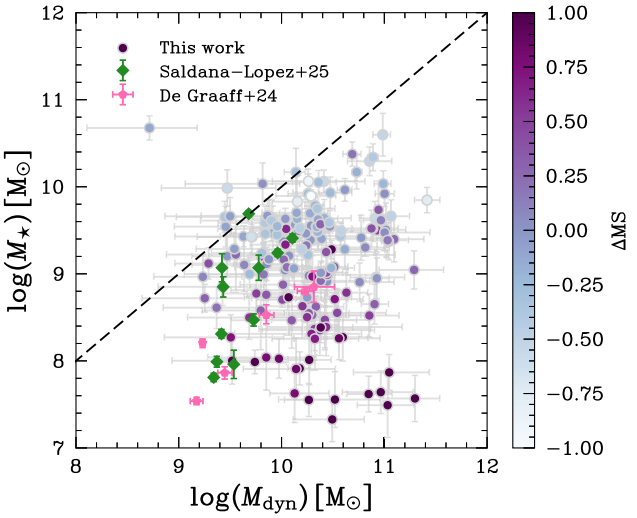

Figure 1. Comparison of the dynamical masses ($M_{\rm dyn}$) inferred from our modelling of grism data and the stellar masses ($M_\star$) inferred from SED fitting. We colour-code our galaxies based on their offset from the main sequence (ΔMS) as defined by C. Simmonds et al. (2025). The majority of our systems lie below the one-to-one relation (dashed line), consistent with a significant contribution to the dynamical mass from gas and/or DM. Six galaxies lie on the relation, highlighting discrepancies in the different mass estimates. We compare our values to ionised gas measurements from A. de Graaff et al. (2024a) and A. Saldana-Lopez et al. (2025) at similar redshifts.

3 DYNAMICAL MASSES AND TULLY–FISHER RELATION

In this section, we present the dynamical masses of our systems based on our kinematic modelling (Section 3.1), and discuss them within the context of the TFR at high redshift (Section 3.2).

3.1 Dynamical masses

We present our results for the dynamical masses of our galaxies in Fig. 1. We find high dynamical masses spanning $\log(M_{\rm dyn}[{\rm M}_\odot]) = 9 - 11$, with the overall expected trend of increasing $M_{\rm dyn}$ with $M_\star$, reflecting the baryons tracing the underlying gravitational potential. We find a significant scatter in the dynamical masses at fixed stellar mass, indicative of varying gas and DM contents. To investigate the source of this scatter, we colour-code our galaxies by their offset from the MS (ΔMS). We define this offset based on the MS from C. Simmonds et al. (2025), which accounts for mass completeness in a more careful way than the J. S. Speagle et al. (2014) relation used to infer the gas content. We find that galaxies above the MS, which are also typically at lower masses, seem most distant from the 1–1 line, implying a lower stellar contribution to the baryonic and total mass.

We expect the dynamical masses to lie above the stellar masses, as they should also incorporate the gas and DM. We find consistent measurements $M_\star < M_{\rm dyn}$ for the majority of the galaxies

in our sample. We discuss the few systems showing unphysical $M_{\rm dyn} - M_\star$ values in more detail in A. L. Danhaive et al. (2025b), the discrepancy pointing to problems in the modelling of either or both masses. We compare our sample with measurements from A. Saldana-Lopez et al. (2025) and A. de Graaff et al. (2024b) at similar redshifts, and find that they probe the same regions of the parameter space. When combined, these two samples highlight a similar scatter of $M_\star$ at fixed $M_{\rm dyn}$ as found in our sample. Overall, these dynamical masses are the key observable that allows us to derive DM fractions (Section 2). We note that in a recent study, S. Phillips et al. (2025) compare intrinsic kinematic measurements from simulations to mock NIRSpec/Integral Field Unit (IFU) fits, and find that despite biases in the recovered values of $v_{\rm rot}$ and σ_0, the dynamical masses remain relatively robust.

3.2 The Tully–Fisher relation

Local star-forming disc galaxies exhibit a tight relationship between their stellar mass and circular velocity ($v_{\rm circ}$, equation 7), namely the TFR. This relation is typically parametrized as a power law, $M \propto V^a$, or

$$\log M_\star = a\ \log v_{\rm circ} + b, \tag{10}$$

where a is the slope and b is the zero-point offset, and $M_\star$ is in units of $\mathrm{M}_\odot$ and $v_{\rm circ}$ in km s^{-1}. This relation is analogous to the $M_\star - M_{\rm dyn}$ relation from Fig. 1, given the fundamental link between circular velocities and dynamical masses (equation 8) when assuming virial equilibrium. By understanding where our galaxies lie on the TFR plane, we can place constraints on their mass content compared to galaxies at lower redshift.

In order to explore the offset between our sample at $z = 4-6$ and the sTFR at cosmic noon and in the local Universe, we fit equation (10) to our sample with the fixed slope from R. Reyes et al. (2011) at $z \sim 0$ ($a = 3.60$). For our fit, we use the Bayesian inference package EMCEE (D. Foreman-Mackey et al. 2013). EMCEE samples the parameter space using an implementation of the affine invariant ensemble sampler for Markov chain Monte Carlo (J. Goodman & J. Weare 2010), resulting in posterior distributions for the model parameters. Importantly, it allows us to self-consistently fit for the intrinsic scatter $\sigma_{\rm int}$ around the relation, assuming that our adopted uncertainties for the various measurements are reliable. We discuss this assumption in Section 5.2. For the EMCEE fitting, we assume uniform priors for all of the parameters and conduct the MCMC sampling with 50 walkers, a 2000-step burn-in phase, and 10 000 samples. We thin our chains to remove autocorrelation between samples, checking for convergence in the trace plots and in the effective number of independent samples.

We find the following best-fitting parameters for the $\log(M_\star[\mathrm{M}_\odot]) > 8$ sample, where we are more complete:

$$a = 3.60 \text{ (fixed)} \tag{11}$$
$$b = 0.76 \pm 0.07 \tag{12}$$
$$\sigma_{\rm int} = 0.49 \pm 0.06. \tag{13}$$

We plot the results for this fiducial fit at $z \sim 5$ in purple in Fig. 2, and also include a fit for the whole sample in red. The large intrinsic scatter, shown by the shaded regions, reflects that the $z \sim 5$ galaxies in our sample are not settled around the TFR. They are likely undergoing kinematic and/or morphological changes on relatively short time-scales, which influence the measured circular velocities at fixed stellar masses. More generally, this

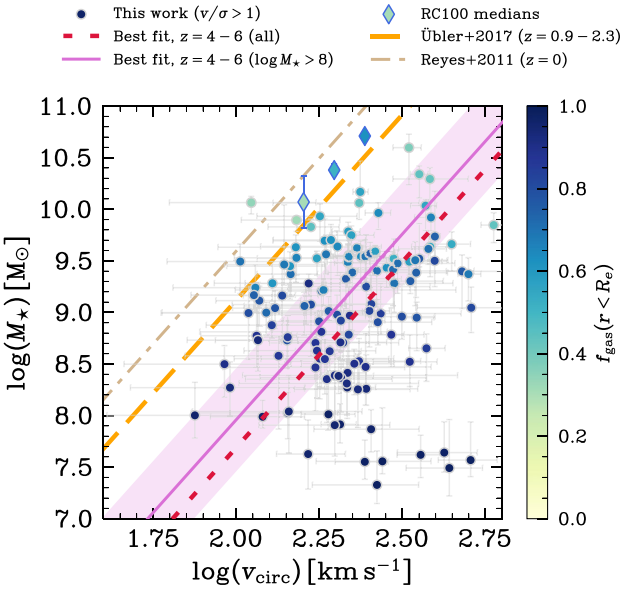

Figure 2. The stellar Tully–Fisher plane for our sample, where the best-fitting linear relation for galaxies with $\log(M_\star[\mathrm{M}_\odot]) > 8$ is shown in solid purple (dotted red for the full sample). The circular velocity ($v_{\rm circ}$) is evaluated at $r_{\rm e}$ with an asymmetricdrift correction. We find that most of our galaxies lie along the relation, albeit with a large scatter, but the lowest-mass galaxies drop off. We compare our measurements at $z \sim 5$ to the relation found for the KMOS$^{\rm 3D}$ $z = 0.9-2.3$ star-forming galaxies from H. Übler et al. (2017) (dashed orange line), and the medians from the RC100 sample (diamonds; A. Nestor Shachar et al. 2023). We also include the TFR at $z \sim 0$ from R. Reyes et al. (2011) for reference (dot–dashed tan curve). We fit our data with the same fixed slope as these works, $a = 3.60$, but compute our own zero-point b. We find $\Delta b \approx -1.3$ dex between $z = 0.9-2.3$ to $z = 4-6$. The large intrinsic scatter around the relation ($\sigma_{\rm int} = 0.49 \pm 0.06$; shaded region) indicates that it is only beginning to emerge at $z \sim 5$.

implies that galaxies have not yet settled into more stable rotating discs, where the TFR is expected to hold (e.g. H. Übler et al. 2017).

Despite the lack of a tight TFR in our sample, we explore the evolution of the zero-point offset b from $z \sim 0$ (R. Reyes et al. 2011) and $z \sim 1-3$ (H. Übler et al. 2017, see also A. L. Tiley et al. 2016) to $z \approx 4-6$. Both works adopt the same slope. We find a significant increase in the zero-point offset, $\Delta b \approx -1.3$ dex, between our TFR and the one measured at cosmic noon (H. Übler et al. 2017). This evolution is more significant than the $\Delta b \approx -0.4$ dex evolution from $z \sim 0$ to cosmic noon. The observed decrease of b with redshift could have (a mixture of) different origins. To visually compare with galaxies at cosmic noon, we plot on Fig. 2 the RC100 sample from A. Nestor Shachar et al. (2023) at $z = 0.6-2.5$. It is clear that these cosmic noon galaxies occupy a different parameter space in the TFR plane, having higher stellar masses ($\log(M_\star[\mathrm{M}_\odot]) \approx 10-11$) and lower gas fractions ($f_{\rm gas} \lessapprox 0.5$) than our sample. It is also important to note that we have fixed the slope to the one reported in R. Reyes et al. (2011), which is calibrated to massive galaxies ($\log(M_\star[\mathrm{M}_\odot]) \gtrapprox 9.5$). Studies have suggested that the sTFR diverges at low masses, and different slopes have been measured when including lower mass galaxies (O. J. Turner et al. 2017; A. Ristea et al. 2024). Specifically, adopting the steeper slope ($a = 5.319 \pm 0.003$) reported in A. Ristea et al. (2024) for the (Mapping Nearby Galaxies at APO) MaNGA

galaxies at $z \sim 0$ could impact our measured zero-point offset evolution.

First, an increase in gas fractions naturally explains the shift of the TFR to higher circular velocities (at fixed mass). This is because $v_{\rm circ}$ reflects the total mass of the galaxy, both baryons and DM, so if the fraction of stars with respect to the other components decreases, the TFR will shift. In the same way, an increase in the DM fractions can also contribute to this shift. It is also possible that b has a mass dependence, since our sample probes smaller masses than the KMOS^{3D} and RC100 samples. It is expected that gas fractions increase at low stellar masses, naturally biasing the stellar TFR. A larger sample spanning larger redshift and mass ranges would be needed to assess the mass dependence of b.

In light of this, we also explore the bTFR in our sample, but similarly to the sTFR we do not find a tight relation akin to what has been measured at cosmic noon and the local Universe (S. S. McGaugh 2012; F. Lelli et al. 2016). We also find a similar offset towards higher circular velocities at fixed baryonic mass. In fact, by fixing the slope to the F. Lelli et al. (2016) slope ($a = 3.75$) at $z \sim 0$, we find $\Delta b = -1.16$ dex, slightly lower than that of the sTFR. However, due to the large scatter in the measured bTFR relation, this zero-point offset is not a robust measurement and only offers a qualitative comparison. Together, these points suggest that DM contributes significantly to the total mass of the galaxies in our sample. This is in contrast to the baryon-dominated galaxies seen at cosmic noon. To correctly measure the bTFR, gas masses would need to be directly measured, which is beyond the scope of this work and our available data.

In terms of intrinsic scatter for the sTFR ($\sigma_{\rm int} = 0.49 \pm 0.06$), we find that it is roughly twice that reported at cosmic noon ($\sigma_{\rm int} = 0.22$; H. Übler et al. 2017), where they also find an increase with respect to the local Universe ($\sigma_{\rm int} = 0.10 - 0.13$; R. Reyes et al. 2011). As discussed in H. Übler et al. (2017), one reason for this could be the fact that galaxies at high-redshift are less settled (R. C. Simons et al. 2016), and are seen more often in non-equilibrium states (M. D. Covington et al. 2010). Also, we rely on 2D grism data in this work and, hence, suffer from more uncertainties than studies with 3D kinematic data. Furthermore, galaxies at high redshift are smaller and lower mass on average, which makes their kinematics more difficult to constrain.

Finally, we note that the lowest-mass galaxies in our sample, with $\log(M_\star[{\rm M}_\odot]) < 8$, distinctively fall off our best-fit relation, with high circular velocities of $v_{\rm circ} > 150$ km s^{-1} despite their low masses. We also fit our full sample, including these $\log(M_\star[{\rm M}_\odot]) < 8$ objects, and find a smaller zero-point ($b = 0.59 \pm 0.08$) and a larger intrinsic scatter ($\sigma_{\rm int} = 0.73 \pm 0.07$). These galaxies also have gas fractions close to 1, and are most likely undergoing starbursts ($\Delta{\rm MS} > 0$). It is possible that the circular velocities measured for these systems have a non-negligible contribution from non-circular motions, such as radial inflows and/or outflows of gas. This would also contribute to the large observed scatter. Due to their low stellar masses and, hence, small spatial extent, such effects would be difficult to detect in our modelling. Our sample is in general not complete, so our discussion regarding the TFR aims at comparing our sample's physical properties with those of galaxies at lower redshift and not fully defining the TFR at $z = 4 - 6$.

4 THE GAS AND DM CONTENT AT $z > 5$

In this section, we quantify the baryonic and DM content of galaxies at $z = 4 - 6$, using gas and DM fractions derived from our kinematic modelling (Section 2). We first study the dependence of these fractions on stellar mass (Section 4.1), then we focus on the relation between DM fractions and baryonic surface density in Section 4.2. Finally, we put our findings in the context of works at lower redshift to discuss the redshift evolution of DM fractions (Section 4.3).

4.1 Baryon content at $z \sim 5$

Fig. 3 shows the inferred gas ($f_{\rm gas}$) and DM ($f_{\rm DM}$) fractions as a function of stellar mass for the galaxies in our samples. We note that $f_{\rm gas}$ is defined relative to the baryonic mass (stars + gas), whereas $f_{\rm DM}$ is defined relative to the total mass (DM + baryons). We fit both relations with a power law of the form

$$f(z, M_\star) = 1 - 10^{\alpha(\log M_\star - 9) + \beta + \gamma(\frac{1+z}{6})}, \quad (14)$$

where α and γ parametrize the mass and redshift dependence, respectively, and β is the normalization at $\log(M_\star[{\rm M}_\odot]) = 9$ and $z = 5$. The power-law shape is consistent with the equation from L. J. Tacconi et al. (2020) for the gas fractions. Similarly to the TFR, these fits are done with EMCEE using the same general set-up (see Section 3). We summarize the best-fitting parameters for both the gas and the DM fractions in Table 1. For the gas fractions, we are not able to constrain the intrinsic scatter ($\sigma_{\rm int}$) around the best-fitting relation. As explained in Section 2, we compute the uncertainties on $f_{\rm gas}$ by propagating the uncertainties on both our input parameters and the constant parameters of the L. J. Tacconi et al. (2020) scaling relation. This yields relatively large uncertainties of the order of $\Delta f_{\rm gas} \approx 0.1$ (see characteristic error in Fig. 3). On the other hand, the outputs $f_{\rm gas}$ from the scaling relation vary only a small amount at fixed mass. This is in part due to the small range probed in terms of ΔMS in our sample, since we are not sensitive to galaxies well below the MS. Because of this, our uncertainties are significantly larger than the scatter shown by our inferred $f_{\rm gas}$, meaning that we cannot constrain $\sigma_{\rm int}$.

4.1.1 Gas fractions

As described in Section 2, we cannot measure gas masses directly, so we infer them based on the galaxies' SFRs, stellar masses, and redshifts through the L. J. Tacconi et al. (2020) scaling relation. As seen in the top panel of Fig. 3, our galaxies have high predicted gas fractions $f_{\rm gas} = M_{\rm gas}/M_{\rm bar}$, with almost all galaxies having $f_{\rm gas} > 0.5$. These systems have more gas than stars in their central region $r < r_{\rm e}$. These high gas fractions are driven in part by the high SFRs, since gas must accrete on to the galaxy to cool and fuel star formation. Gas fractions are also expected to be overall higher at high redshift, but we cannot constrain the redshift dependence of $f_{\rm gas}$ due to the small redshift range probed in this work. However, as expected, our inferred dependence of $\gamma = -0.36 \pm 0.45$ is consistent with its counterpart in the L. J. Tacconi et al. (2020) scaling relation ($D = -0.41 \pm 0.03$), albeit with very large uncertainties.

We compare our gas fractions with estimates at cosmic noon from R. Genzel et al. (2020) and A. Nestor Shachar et al. (2023), which show a large scatter at $\log(M_\star[{\rm M}_\odot]) \approx 10 - 11$. Because

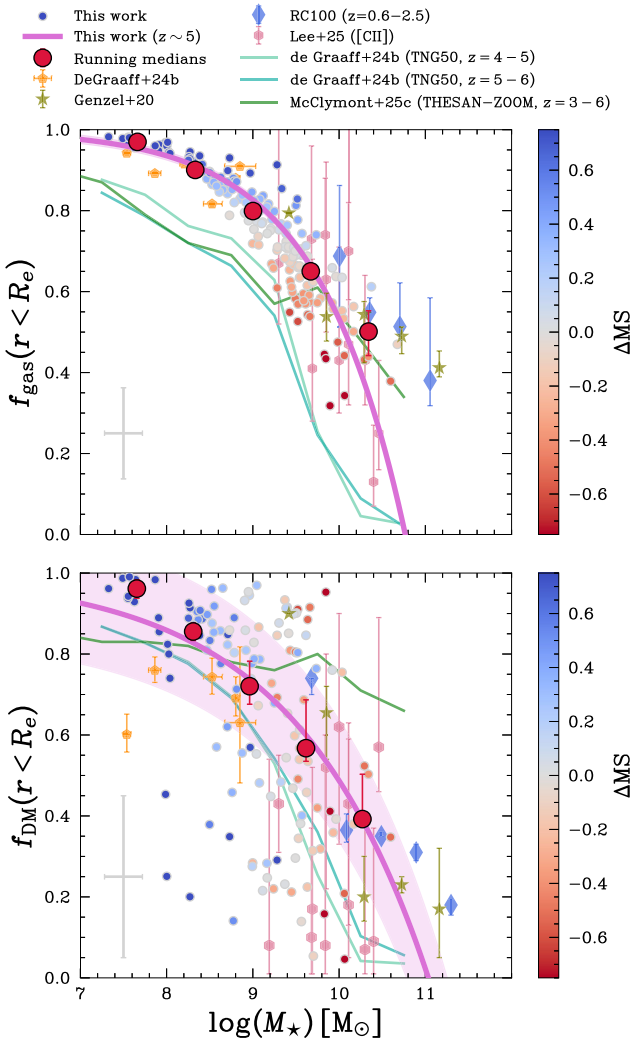

Figure 3. Gas (top) and DM (bottom) fractions (within r_e) as a function of stellar mass, with the characteristic uncertainty shown in grey. The $f_{\rm gas}(r < r_e)$ (equation 4) is computed using the sSFR, redshift, and stellar mass of each galaxy following L. J. Tacconi et al. (2020). The $f_{\rm DM}(r < r_e)$ is computed using $M_{\rm gas}$ along with $M_{\rm dyn}$ and $M_\star$ as shown in equation (9). We fit our data with a power law (solid purple line) for both relations, showing the intrinsic scatter (shaded region) only for $f_{\rm DM}$. We cannot constrain $\sigma_{\rm int}$ for $f_{\rm gas}$ due to the inferred uncertainties being significantly larger than the scatter in the outputs of the L. J. Tacconi et al. (2020) scaling relation for our sample (see Section 4.1.1). We compare our results with measurements from R. Genzel et al. (2020) (green stars) and A. Nestor Shachar et al. (2023) (RC100; blue diamonds) at cosmic noon and A. de Graaff et al. (2024a, 2024b) (orange pentagons) and L. L. Lee et al. (2025) (pink hexagons) at high redshift. For most of our sample, we find high gas and DM fractions $f > 0.5$. We find relatively good agreement with median trends from the THESAN-ZOOM simulations (green solid line; W. McClymont et al. 2025c) and the TNG50 simulations (blue solid lines; A. de Graaff et al. 2024b).

there is little overlap between this mass range and the one probed in this work, a direct comparison to quantify the independent effects of redshift is not possible. However, their results are consistent with a decrease, on average, of gas fractions with stellar mass.

The high gas fractions at high-redshift are consistent with other predictions of the increase of gas fractions with redshift (G. Cresci et al. 2009; R. Genzel et al. 2015; A. Pillepich et al. 2019). However, this effect appears to also have a strong mass component. The gas fractions found in A. de Graaff et al. (2024a, 2024b) at $z \approx 6-8$ are consistent with our results. In fact, although A. de Graaff et al. (2024a) use the local relation from J. Kennicutt (1998) to infer gas masses from SFRs, their measurements lie nicely along our best-fitting relation. This suggests that this local relation holds well at $z \sim 6$, at least at the low masses ($\log(M_\star[M_\odot]) < 9$) probed by their work. The lower gas fractions presented in L. L. Lee et al. (2025), derived from the Atacama Large Millimeter/submillimeter Array (ALMA) Band-7 dust-continuum measurements (see appendix C in L. L. Lee et al. 2025) at $z \sim 4-6$, are consistent with our best-fitting power law.

The steep mass dependence of $f_{\rm gas}$ on $M_\star$ is also seen in the TNG50 simulations (A. Pillepich et al. 2019; A. de Graaff et al. 2024b) and the THESAN-ZOOM simulations (R. Kannan et al. 2025; W. McClymont et al. 2025c). At low masses, we find higher gas fractions on average than both of these simulations. This is partly because the relations from L. J. Tacconi et al. (2020) and J. S. Speagle et al. (2014) do not reach the low mass [$\log(M_\star[M_\odot]) < 9$] end, and hence the extrapolation could cause an overestimate of gas fractions at low masses. Additionally, our sample is biased to very star-forming galaxies at the low-mass end, which naturally explains our higher medians. Finally, the lower gas fractions reported in the simulations could imply an overestimation of the strength of baryonic feedback in low-mass galaxies.

Table 1. Summary of the parameters for the power-law fit (equation 14) to the $f_{\rm gas}-M_\star$ and $f_{\rm DM}-M_\star$ relations (Fig. 3). We cannot constrain $\sigma_{\rm int}$ for the $f_{\rm gas} - M_\star$ relation due to the inferred uncertainties on $f_{\rm gas}$ being significantly larger than the scatter in the outputs of the L. J. Tacconi et al. (2020) scaling relation for our sample (see Section 4.1.1 for more details).

Parameter	$f_{\rm gas}$	$f_{\rm DM}$
α	0.43 ± 0.03	0.28 ± 0.05
β	-0.73 ± 0.03	-0.57 ± 0.04
γ	-0.36 ± 0.45	0.34 ± 0.65
$\sigma_{\rm int}$	–	0.15 ± 0.02

4.1.2 *DM fractions*

We now discuss the bottom panel of Fig. 3, where we plot our DM fractions (equation 9) as a function of stellar mass. These fractions are computed within the half-light, or effective, radius r_e of the Hα emission to avoid extrapolations of our kinematic measurements to larger radii. This implies that the fractions discussed in this work are relevant for the central $r = 1.20 \pm 0.05$ kpc of each galaxy (sample median; A. L. Danhaive et al. 2025a). We see a large scatter in the DM content of galaxies at fixed stellar mass, but none the less find that low-mass galaxies ($\log(M_\star[M_\odot]) < 9$) are predominantly DM dominated with $f_{\rm DM}(r < r_e) > 0.5$. Above $\log(M_\star[M_\odot]) = 9$, we observe a larger scatter and an overall decline in DM fractions with stellar mass, as is highlighted by the running medians and our best-fitting power law in Fig. 3. We colour-code our galaxies by their offset from the main sequence, but we do not find a clear trend.

We put our $f_{\rm DM}$ measurements in the context of works at cosmic noon, which probe a higher mass range $\log(M_\star[M_\odot]) \approx 10-11$. As shown in Fig. 4, R. Genzel et al. (2020) find that star-forming galaxies at cosmic noon have baryon-dominated cores, with $f_{\rm DM} \lessapprox 0.5$. This is consistent with the extrapolation of our

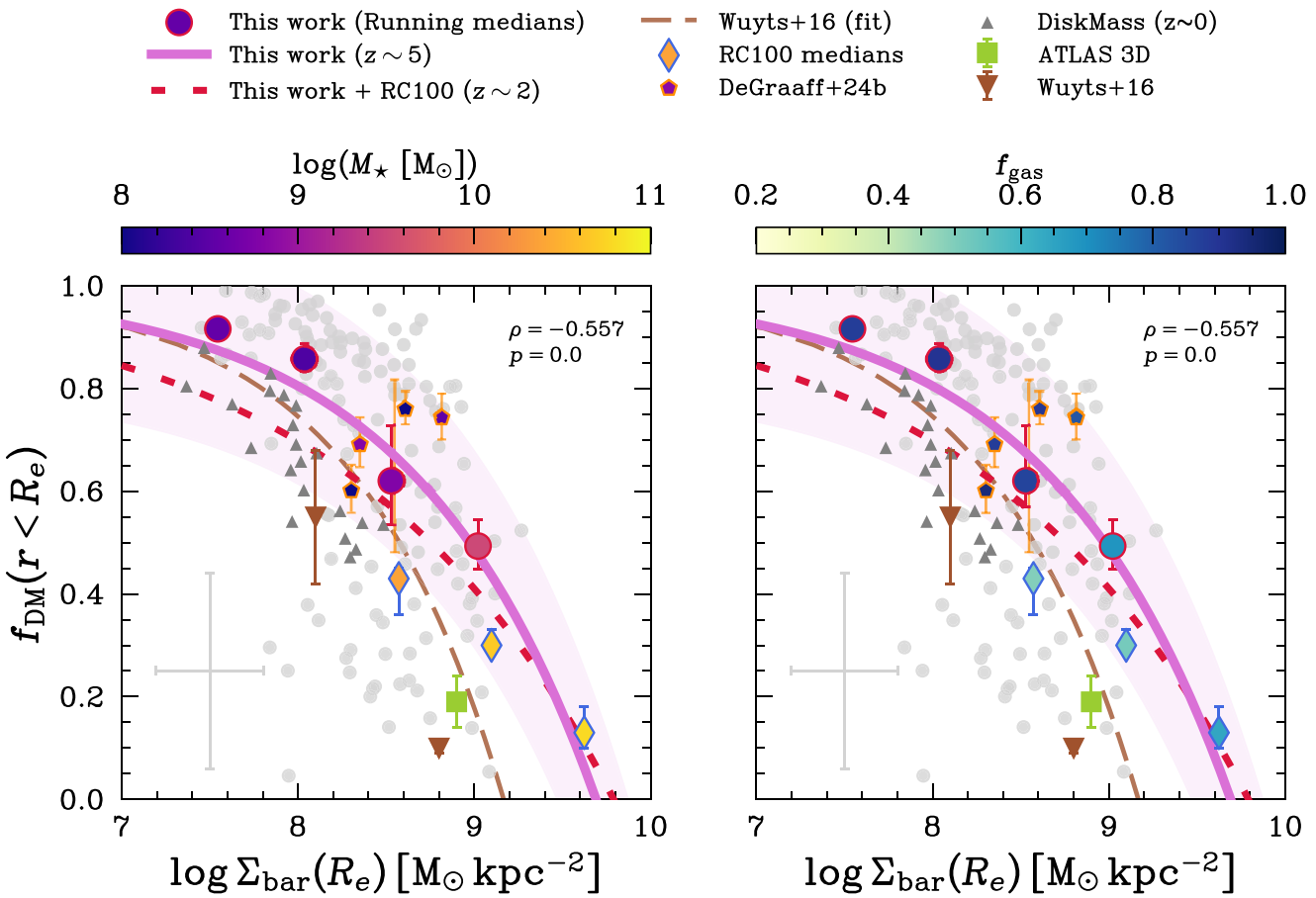

Figure 4. DM fraction as a function of baryonic surface density ($\Sigma_{\rm bar}$) for our sample (circles) and samples at lower (diamonds; A. Nestor Shachar et al. 2023) and similar to higher (pentagons; A. de Graaff et al. 2024b) redshift. We colour-code points by stellar mass (left panel) and gas fractions (right panel). We show the characteristic uncertainty for our sample in grey. We find a strong negative correlation between $f_{\rm DM}$ and $\Sigma_{\rm bar}$ ($\rho = -0.551$, $p < 0.001$), with a best-fitting relation (solid purple line) steeper than S. Wuyts et al. (2016) at cosmic noon (dashed brown line), and with an offset. We also plot the best-fitting relation obtained when fitting our points with those from A. Nestor Shachar et al. (2023) (dashed–dotted red line). For comparison, we plot medians from ETGs at $z \sim 0$ from the ATLAS3D survey (purple square; M. Cappellari et al. 2013a) and LTGs from the DiskMass Survey (grey triangles; T. P. K. Martinsson et al. 2013). Our galaxies agree with A. Nestor Shachar et al. (2023) at low fractions $f_{\rm DM} < 0.5$, but lie above the relation at high fractions. The galaxies in our sample are smaller, less massive, and more gas-rich than those probed at cosmic noon, driving the apparent shift in the relation.

power-law fit to these high masses, suggesting that the mass dependence of $f_{\rm DM}$ exists independently of redshift. In fact, A. de Graaff et al. (2024b) show with the TNG simulations that the baryon fraction within 1 kpc, $f_{\rm bar}(r < 1\ \mathrm{kpc})$, remains constant with redshift at fixed mass. However, it is important to note that our measurements are not at fixed apertures, and we need to take into account the redshift evolution of galaxy sizes (T. Shibuya, M. Ouchi & Y. Harikane 2015; E. Ward et al. 2024; N. Allen et al. 2025; L. Yang et al. 2025; A. L. Danhaive et al. 2025a). None the less, our findings suggest that the high DM fractions seen at high-z, both in this work and A. de Graaff et al. (2024b), are at least in part driven by the lower stellar masses probed compared to lower redshifts. In fact, L. L. Lee et al. (2025) probe higher stellar masses on average ($\log(M_\star[\mathrm{M}_\odot]) > 9$) and find DM fractions ranging from $f_{\rm DM} \approx 0.1$ to $f_{\rm DM} \approx 0.6$, consistent with the scatter seen in our larger sample at those masses. This anticorrelation between DM fractions and stellar mass is consistent with other studies at $z < 3$ (R. Genzel et al. 2020; G. Sharma, P. Salucci & G. van de Ven 2021; G. Sharma et al. 2025), as well as studies of late-type galaxies (LTGs) in the local Universe (e.g. K. Zhu et al. 2024). However, we caution that G. Sharma et al. (2021, 2025) assume molecular gas fractions below 5 per cent which are uncharacteristically low for galaxies at $z \sim 1$ (L. J. Tacconi et al. 2018), and conduct their fitting with a fixed Sérsic index of $n = 1.35$, both of which impact the derived DM fractions.

We also compare our DM fractions with predictions from the THESAN-ZOOM simulations at $z = 3 - 6$. In general, the simulations are consistent with the majority (60 per cent) of our sample having high DM fractions $f_{\rm DM} > 0.5$. However, W. McClymont et al. (2025c) find a weaker mass trend, which does not reproduce the population of $\log(M_\star[\mathrm{M}_\odot]) > 9$ galaxies with lower $f_{\rm DM}$. This could point to mechanisms that drive DM out from the central regions, such as intense feedback from star formation or black holes (see Section 5 for more discussion). Within the simulations, this could also be due to a decrease in the number of galaxies at the high-mass end. Our observed dependence of $f_{\rm DM}$ on $M_\star$ is instead more consistent with the trend observed in the TNG50 simulations (A. de Graaff et al. 2024b).

Some objects have high DM fractions close to $f_{\rm DM} = 1$. Although these could be caused by an overestimate of the dynami-

Table 2. Summary of the parameters for the power-law fit to the $f_{DM} - \Sigma_{bar}$ relation (where the parameters are defined as in equation 14), as shown on Fig. 4.

Fit	This work	This work + RC100
α	0.48 ± 0.08	0.28 ± 0.02
β	-0.28 ± 0.04	-0.33 ± 0.02
γ	-0.05 ± 0.58	-0.38 ± 0.07
σ_{int}	0.12 ± 0.03	0.11 ± 0.01

cal mass, they can also point to steepening of the DM halo density profile in the central regions of these galaxies. We explore this in Section 5.1. We also find that the inferred f_{DM} fractions for 20 per cent of our sample are unphysical, i.e., $f_{DM} < 0$. Negative fractions imply that the baryonic mass is larger than the dynamical mass, which could be caused by one or more of the following. The stellar mass inferred from SED fitting could be overestimated (e.g. due to outshining effects, Section 5.2), the dynamical mass from the kinematics fitting could be underestimated, or the gas fractions inferred from the L. J. Tacconi et al. (2020) empirical relation could be overestimated. Many galaxies in our sample, despite having good fits with low residuals, have clumpy morphologies, which could indicate clumpy SF and/or final stages of a merger. Irregular morphologies can bias the measurement of the rotational velocity due to the simplistic nature of the rotation curve model. Also, if a merger is in fact taking place, the stellar mass may be overestimated due to the multiple-system nature of the object. In some of the systems, the PROSPECTOR posteriors for the stellar mass are distinctively double-peaked, with a lower mass solution that would boost the f_{DM}. Finally, based on the PROSPECTOR-inferred SFHs, many of the systems are either in a burst or just went through a burst, with a peak in SF over a $\sim 5 - 10$ Myr time-scale. Especially at low masses, these starbursts can disrupt the ordered rotation of the gas, leading to low and/or biased measurements of v_{rot}.

4.2 Baryonic surface density

In order to investigate the origin of the DM fractions measured in our $z = 4 - 6$ sample, we study their correlation with the baryonic surface density Σ_{bar}, computed within the effective radius of the Hα emission, r_e

$$\Sigma_{bar}(r_e) = \frac{M_{bar}(r < r_e)}{2\pi r_e^2}. \quad (15)$$

Our results are shown in Fig. 4, colour-coded by the stellar mass and the gas fraction. The baryonic surface densities of our galaxies span a narrow range of $\log(\Sigma_{bar})[M_\odot\ kpc^{-2}] \approx 8 - 9$. We find a strong anticorrelation between f_{DM} and $\log \Sigma_{bar}$, with a Spearman rank correlation coefficient of $\rho = -0.557$ and p-value of $p < 0.001$.

We fit our $f_{DM} - \log \Sigma_{bar}$ relation with a power law, replicating the one used for the $f_{DM} - \log(M_\star[M_\odot])$ (equation 14). This parametrization is motivated by studies of this relation at lower redshift (S. Wuyts et al. 2016; R. Genzel et al. 2017; A. Nestor Shachar et al. 2023), to provide a more straightforward comparison. We present our best-fitting parameters in Table 2 and plot our best-fitting relation in Fig. 4. It is clear that our sample does not follow a clear power-law shape, which is also highlighted by the large intrinsic scatter $\sigma_{int} = 0.12 \pm 0.03$. The fit is also driven by the higher f_{DM} , which has smaller uncertainties. This causes most of our lower f_{DM} values to have smaller Σ_{bar} than predicted by the best-fitting curve.

The tight relation between DM fraction and Σ_{bar} has been found to hold out to cosmic noon in observations (S. Wuyts et al. 2016; R. Genzel et al. 2020; A. Nestor Shachar et al. 2023; G. Sharma et al. 2025) as well as in simulations (H. Übler et al. 2021). This trend links the baryons with underlying the DM, and could be explained by a few different phenomena. The high baryon densities could drive out the DM in the central region through heating. Also, the high densities could be induced by a change in the size of the galaxy. In general, for a fixed DM halo and at fixed stellar mass, a higher density of baryons in the centre will naturally result in a lower DM fraction when compared to the same galaxy but more diffuse. At $z \sim 1$, B. I. Ciocan et al. (2025) find a correlation between f_{DM} and the stellar mass surface density, which is consistent with a toy model derived directly from the TFR (H. Übler et al. 2017; N. F. Bouché et al. 2022).

Our measured correlation ($\rho \approx 0.56$) is weaker than the one reported by A. Nestor Shachar et al. (2023) at $z \sim 2$ ($\rho = 0.64$) and $z \sim 1$ ($\rho = 0.84$). The weakening of the correlation with redshift, as was already observed at cosmic noon, points to an increase in galaxy-to-galaxy diversity. In Fig. 4, we plot the best-fitting relation from S. Wuyts et al. (2016), and we find that our galaxies with the highest DM fractions lie above this relation, as also highlighted by our best-fitting relation. At lower DM fractions, our sample aligns better with the relation.

We also perform a fit combining our $z = 4 - 6$ data with the $z = 1 - 2.5$ RC100 data from A. Nestor Shachar et al. (2023) to obtain better constraints for the redshift evolution of the $f_{DM} - \Sigma_{bar}$ relation. Our best-fitting parameters are shown in Table 2. In our initial fit, the redshift dependence was poorly constrained ($\gamma = -0.05 \pm 0.58$), but when we include the RC100 data, we can constrain the increase of f_{DM} with redshift ($\gamma = -0.38 \pm 0.07$). We investigate the origin of this increase of f_{DM} at fixed Σ_{bar} through the colour-coding by $M_\star$ and f_{gas} in the two panels of Fig. 4, and comparing our sample to the A. Nestor Shachar et al. (2023) sample at cosmic noon. We do not colour-code by r_e because there is little overlap in sizes between the two samples, with our galaxies spanning $r_e \approx 0.3 - 3$ kpc and the RC100 sample $r_e \approx 3 - 10$. The RC100 sample has masses $\log(M_\star[M_\odot]) \approx 10 - 11$, gas fractions typically $f_{gas} \lessapprox 0.8$, and $r_e > 3$ kpc. It is clear that our sample occupies a different parameter space, with lower masses, higher gas fractions, and smaller sizes. Interestingly, our baryonic surface densities $\log \Sigma_{bar} \approx 8 - 9$ have significant overlap with those of cosmic noon galaxies. This implies high densities Σ_{bar} at high redshift, in part driven by the smaller sizes r_e (e.g. T. Shibuya et al. 2015; E. Ward et al. 2024). In addition, the gas content is higher and more centrally concentrated, further increasing the baryonic densities in the inner regions. The shift to higher f_{DM} at fixed Σ_{bar} could therefore be driven by the smaller stellar masses, a direct consequence of the stellar-to-halo-mass relation where $M_\star/M_{halo}$ decreases with decreasing $M_\star$ (P. S. Behroozi et al. 2010, 2019; B. P. Moster et al. 2010; S. Tacchella et al. 2018).

The high baryonic surface densities within r_e at high redshift are consistent with the build-up of bulges. In A. L. Danhaive et al. (2025a), the study of multiwavelength sizes and their ratios at $z \sim 5$ supports the growth of galaxies through central starbursts instead of smooth inside-out growth. This is consistent with bulges forming in these relatively low-mass galaxies. At cosmic noon, star-forming galaxies have been shown to predominantly grow inside-out (E. J. Nelson et al. 2016), consistent with stars forming in gas discs around an older stellar bulge. The formation of these

stellar discs is also reflected in the rapid increase of sizes (r_e) at cosmic noon (T. Shibuya et al. 2015). In this context, the decrease of f_{DM}, at fixed Σ_{bar}, with cosmic time reflects the mass build-up of bulges which begin to dominate the central regions of the galaxy. Also, the baryons extend further out into the halo, through inside-out growth, where the DM density decreases, which further decreases f_{DM}.

Assuming galaxies grow along the SFMS, a $\log(M_\star[M_\odot]) = 9$ galaxy from our sample at $z \sim 5$ would grow to $\log(M_\star[M_\odot]) \approx 10.5 - 11$ by cosmic noon, similar to the RC100 galaxies. If they maintain high DM fractions in their cores, they would evolve into a separate population from these cosmic noon galaxies, more akin to late-type galaxies (LTGs) in the local Universe (M. Barnabè et al. 2012; T. P. K. Martinsson et al. 2013). The sub-set of the galaxies in our sample with $f_{DM} < 0.5$ would instead be candidate progenitors for the baryon-dominated galaxies at cosmic noon, having also similar gas fractions, as they occupy a similar region on the $f_{DM} - \Sigma_{bar}$ plane. As discussed in A. Nestor Shachar et al. (2023), these galaxies are expected to become ETGs seen in the local Universe (M. Cappellari et al. 2013a). These different evolutionary tracks are consistent with the large scatter seen in our sample, suggesting a variety of different populations. However, DM fractions are not expected to stay constant within a galaxy's evolutionary track. In fact, their dependence on mass (Fig. 3) implies that as galaxies grow, their DM fraction changes. Also, the effective radii increase with cosmic time, which also affects the measurements. We investigate the redshift evolution of f_{DM} in the next section.

4.3 Redshift evolution of f_{DM}

In Fig. 5, we plot our inferred DM fractions as a function of redshift. We plot our sample medians at $z = 4.5$ and $z = 5.5$, for the lower-mass ($\log(M_\star[M_\odot]) < 9$) and higher-mass ($\log(M_\star[M_\odot]) > 9$) galaxies. Although our sample spans a wide range of f_{DM}, we find high fractions on average ($f_{DM} > 0.5$). For the high-mass galaxies, with median $\log(M_\star[M_\odot]) = 9.5$, we find $f_{DM} = 0.51^{+0.17}_{-0.03}$ and $f_{DM} = 0.55^{+0.06}_{-0.01}$ at $z = 4.5$ and $z = 5.5$, respectively. For the low-mass galaxies, with median $\log(M_\star[M_\odot]) = 8.5$, we find $f_{DM} = 0.81^{+0.04}_{-0.19}$ and $f_{DM} = 0.65^{+0.13}_{-0.20}$. In both cases, we do not see evidence for a redshift evolution, as our medians at $z = 4.5$ and $z = 5.5$ are consistent within the uncertainties. This is expected given our poorly constrained γ values (Table 1).

We now place our measurements in the context of work at cosmic noon and the local Universe. In the same redshift range $z \approx 4 - 6$, L. L. Lee et al. (2025) report a wide range of f_{DM} for their higher mass sample ($\log(M_\star[M_\odot]) \approx 9 - 10.5$), but their higher f_{DM} systems are consistent with our high-mass medians. However, they also report galaxies that have large baryon contents ($f_{DM} \lessapprox 0.2$). We also find similar systems in our sample (Fig. 3) even though our medians lie at higher f_{DM}. The systems from L. L. Lee et al. (2025) are therefore consistent with being a sub-set of the more extensive population probed in this work. At higher redshift ($z \approx 5 - 8$), measurements from A. de Graaff et al. (2024a, 2024b), who find $f_{DM} > 0.5$ for their sample of $\log(M_\star[M_\odot]) \approx 8 - 9$, are broadly consistent with our low-mass medians. On the other hand, the medians for $\log(M_\star[M_\odot]) \approx 10 - 11$ galaxies at cosmic noon (R. Genzel et al. 2020; A. Nestor Shachar et al. 2023) show low DM fractions ($f_{DM} \approx 0.2 - 0.4$). When combining all of these measurements together, the resulting picture suggests that mass plays a significant role in determining the DM content within the central regions of galaxies. The massive systems at cosmic noon are predominantly baryon-dominated, as is also seen in more massive systems at $z \sim 5$. On the other hand, low-mass galaxies seem more DM-dominated. This mass dependence is consistent with findings for LTGs in the local Universe, whereas ETGs remain predominantly baryon-dominated independently of mass (M. Cappellari et al. 2013a; T. P. K. Martinsson et al. 2013; K. Zhu et al. 2024).

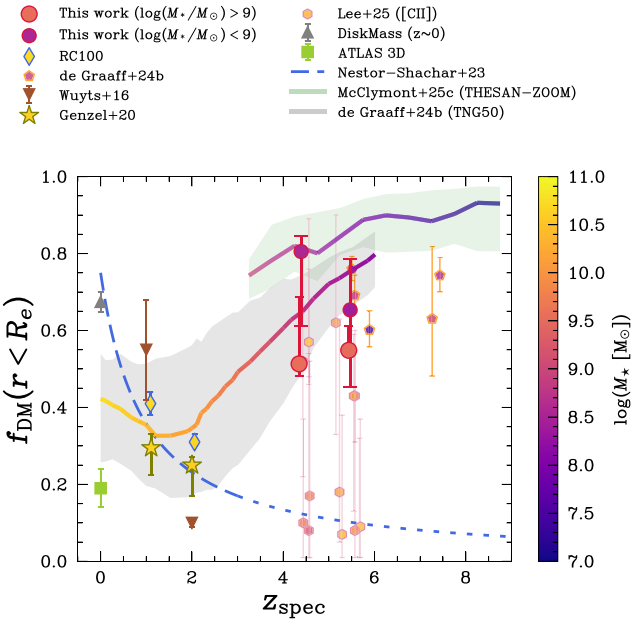

Figure 5. DM fraction as a function of redshift for our sample (circles) and samples from the literature (T. P. K. Martinsson et al. 2013; M. Cappellari et al. 2013a; S. Wuyts et al. 2016; R. Genzel et al. 2020; A. Nestor Shachar et al. 2023; A. de Graaff et al. 2024a, 2024b; L. L. Lee et al. 2025). We plot the evolution measured in A. Nestor Shachar et al. (2023) (dashed blue line), and its extrapolation to $z > 2.5$ (dotted blue line). Our sample medians lie well above those at cosmic noon, although our sample shows large diversity in f_{DM} and probes $\sim 2 - 3$ dex lower stellar masses. Qualitatively, we compare our medians ($\log(M_\star[M_\odot]) \approx 9$) with the median evolution of $f_{DM}(r < r_e)$ for TNG50 galaxies (A. de Graaff et al. 2024b) selected at $z = 6$ with $8 < \log(M_\star[M_\odot]) < 9$ (thick line with 16th and 84th percentiles shown in the grey shaded region). Similarly, we plot the median evolution for THESAN-ZOOM galaxies (W. McClymont et al. 2025c) with $\log(M_\star[M_\odot]) = 7 \pm 0.5$ at $z = 9$ (thick line with 16th and 84th percentiles shown in the green shaded region). Although we expect redshift evolution of $f_{DM}(< r_e)$ due to the evolution of sizes with redshift, the strong dependence of stellar mass is evident here.

To further investigate this, we plot the median tracks from the TNG50 (A. de Graaff et al. 2024b) and THESAN-ZOOM (W. McClymont et al. 2025c) simulations. Specifically, for TNG50, we plot the median evolution of $f_{DM}(r < r_e)$ for galaxies selected at $z = 6$ with $8 < \log(M_\star[M_\odot]) < 9$. The THESAN-ZOOM track is computed as a median from galaxies with $\log(M_\star[M_\odot]) = 7 \pm 0.5$ at $z = 9$. This comparison with simulations is qualitative, as the radii r_e are defined and measured differently in observations and simulations. Observationally, we are only able to measure the 2D half-light radius, whereas simulations define r_e as the 3D stellar half-mass radius. The choice of r_e will have an impact on the measured fractions and the derived comparisons. Despite this not being an apples-to-apples comparison, it is informative to explore its implications.

As discussed in A. de Graaff et al. (2024b), TNG50 predicts that low-mass galaxies are DM dominated at every epoch, and the observed evolution of f_{DM} is driven by the masses probed.

In fact, the tracks on Fig. 5 show that a single galaxy goes from being DM-dominated at $z \sim 6$ to being baryon-dominated at $z \sim 2$. This is also consistent with the tracks from THESAN-ZOOM, although these simulations only reach $z = 3$. This has strong implications for the evolutionary tracks of galaxies, since it suggests that the DM-dominated low-mass galaxies probed at high redshift are direct progenitors of the baryon-dominated cosmic noon galaxies. From cosmic noon, the DM-dominated systems settle as the DM-dominated LTGs in the local Universe, whereas the baryon-dominated systems could deplete their gas and settle into the ETGs (A. Nestor Shachar et al. 2023). A detailed forward modelling of the simulations is needed to conduct a better comparison with the increasing number of observed fractions.

5 DISCUSSION

The study of DM fractions, within the effective radius, at cosmic noon ($z \approx 1-3$) unveiled that the massive ($\log(M_\star[\mathrm{M}_\odot]) = 10-11$) star-forming galaxy population is predominantly baryon-dominated (R. Genzel et al. 2017, 2020; A. Nestor Shachar et al. 2023). In this work, we push the study of $f_{\rm DM}$ to $z \approx 4-6$, where we are directly probing progenitors of these cosmic noon systems. In Sections 4.1 and 4.2, we presented our DM fractions and their dependence on stellar mass and baryonic surface density, investigating the physical drivers for the offsets we observe with respect to cosmic noon galaxies. In Section 4.3, we put our measured $f_{\rm DM}$ in the context of galaxies across cosmic time and predictions from tracks of cosmological simulations.

In this section, we qualitatively explore what our measurements can teach us about the underlying DM halo, and specifically what constraints we can place on the shape of its density distribution in the central regions (Section 5.1). From this, we hope to shed light on the consistency of different estimations of the galaxy–halo connection. We also discuss the different sources of uncertainties in our baryonic (Section 5.2) and DM (Section 5.3) mass measurements. Finally, we also consider the contribution of BHs to our measured fractions in Section 5.4.

5.1 Empirical model predictions

Our modelling, which is limited to probing rotational curves out to $\approx 1-2r_{\rm e}$, does not allow for a detailed recovery of the underlying DM density profiles of our galaxies. Ideally, rotation should be probed further out to several $r_{\rm e}$. However, the measure of the DM fractions within $r_{\rm e}$ can provide constraints on the DM density profile via comparisons to empirical predictions, which require various assumptions. We explore these constraints in this section, but caution that they remain qualitative and reliant on assumed relations.

The SMHM relation has been studied in detail both in empirical models (S. Tacchella et al. 2018; P. Behroozi et al. 2019) and in simulations (D. Ceverino, S. C. O. Glover & R. S. Klessen 2017; X. Ma et al. 2018), with constraints from observations (A. V. Kravtsov, A. A. Vikhlinin & A. V. Meshcheryakov 2018; G. Girelli et al. 2020; A. B. Romeo, O. Agertz & F. Renaud 2020; M. Shuntov et al. 2022, 2025). This relation links the halo mass of galaxies to their stellar mass at a given redshift, allowing us to estimate the halo masses for the galaxies in our sample. In order to estimate the halo masses for our galaxies, we adopt the P. Behroozi et al. (2019) SMHM relation, which has a double power-law shape with an added Gaussian

$$\log_{10}\left(\frac{M_*}{M_1}\right) = \varepsilon - \log_{10}\left(10^{-\alpha x}+10^{-\beta x}\right) + \gamma \exp\left[-0.5\left(\frac{x}{\delta}\right)^2\right], \tag{16}$$

where $x \equiv \log_{10}\left(\frac{M_{\rm peak}}{M_1}\right)$, $M_{\rm peak}$ is the peak halo mass and M_1 is a characteristic mass. The free parameters M_1, ϵ, α, β, and γ all have redshift-dependent expressions, and δ is a constant. Once we have inferred the halo mass by numerically solving equation (16), we can derive the corresponding virial radius

$$R_{\rm vir} = \left(\frac{4}{3}\frac{\pi 200\rho_c}{M_{\rm halo}}\right)^{-1/3}, \tag{17}$$

since $R_{\rm vir}$ is defined as the radius where the density is 200 times the critical density ρ_c of the Universe at that redshift, and $M_{\rm halo}$ is the DM mass within the virial radius. For the shape of the DM density profile, we assume a generalized Navarro–Frenk–White (NFW; J. F. Navarro, C. S. Frenk & S. D. M. White 1997) profile

$$\rho_{\rm DM}(r) = \frac{\rho_0}{(r/r_s)^\alpha(1+r/r_s)^{3-\alpha}}, \tag{18}$$

where $\alpha = 1$ corresponds to a classic NFW profile. Given these assumptions, we can constrain the value of α needed to reproduce our measured DM fractions $f_{\rm DM}$ within the effective radius. We restrict our values between $\alpha = 0$ and $\alpha = 3$, above (below) which the profile becomes convex (concave) in logarithmic space. In fact, for $\alpha > 3$, equation (18) develops an upturn near $r = r_s$, as the outer slope $(3-\alpha)$ becomes negative. Conversely, when $\alpha < 0$, the inner slope (α) becomes negative, producing a downturn at $r = r_s$. Within the allowed range $0 \leq \alpha \leq 3$, the profile smoothly transitions from a nearly flat core ($\alpha = 0$) to a progressively steeper slope that becomes (log-)linear at $\alpha = 3$.

The only additional unknown is the concentration c, defined as

$$R_{\rm vir} = cR_{\rm s}, \tag{19}$$

where $R_{\rm s}$ is the scale radius. Given our other assumptions, the value of c effectively re-normalizes the predicted DM fractions for all of our systems, increasing them as c increases. DM only simulations predict low concentrations at $z \sim 5$ (A. A. Dutton & A. V. Macciò 2014), so we set $c = 5$.

In Fig. 6, we present the estimated values of α needed to reproduce our measured DM fractions within the effective radius. We find that ≈ 30 per cent of our sample lies below $\alpha = 1$, implying that their DM fractions are best reproduced by a profile that is more cored than the classical NFW. Evidence for DM cores has already been found at cosmic noon (R. Genzel et al. 2020; N. F. Bouché et al. 2022; A. Nestor Shachar et al. 2023; B. I. Ciocan et al. 2025), where samples are predominantly baryon-dominated and require cored profiles to reproduce their low $f_{\rm DM}$. Aside from more extreme solutions such as the modification of the nature of DM (W. Hu et al. 2000; E. Calabrese & D. N. Spergel 2016) or of our gravity model (M. Milgrom 1983), a more natural explanation for such cores is a strong interaction between the baryons and the DM within galaxies. Specifically, this would require kinetic heating of the DM in the central regions to drive it outwards. This could be achieved through effective feedback mechanisms from star formation and BHs. Another possibility is that some of these low $f_{\rm DM}$ galaxies are in a post-merger phase, with disturbed kinematics and diffused DM haloes. This is plausible given that most of the galaxies in the $\alpha < 0$ region have higher stellar masses ($\log(M_\star[\mathrm{M}_\odot]) > 9$).

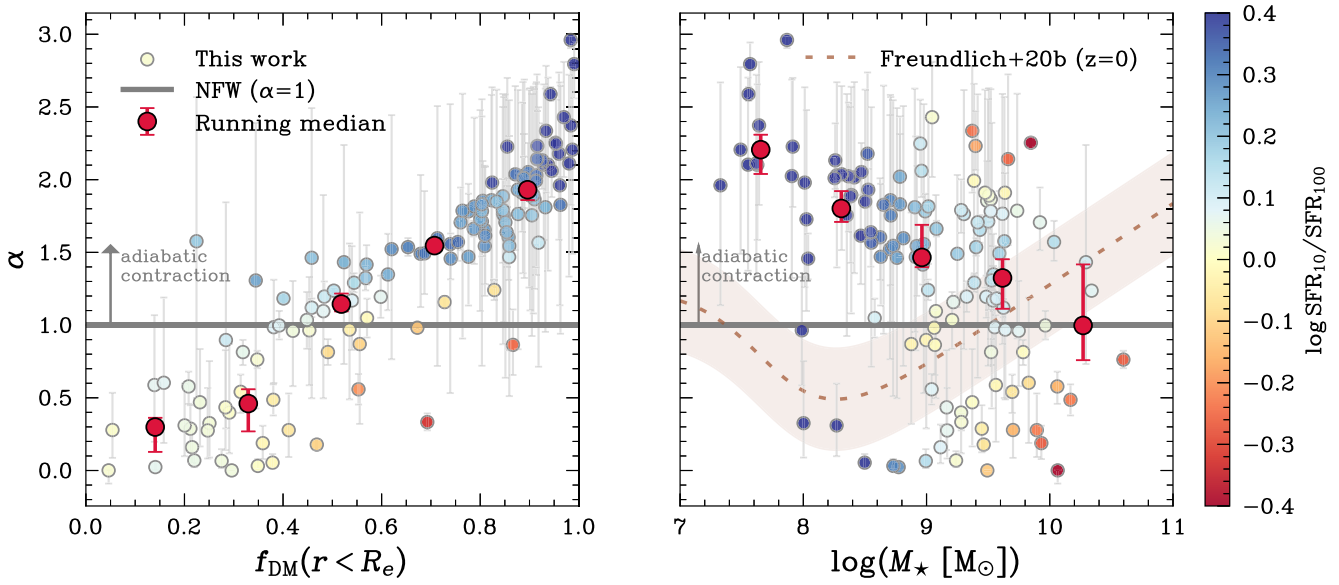

Figure 6. Estimated slope α of the inner DM density profile for a modified NFW distribution (equation 18) as a function of measured DM fractions (left) and stellar mass (right). A value of $\alpha = 1$ represents the classical NFW profile, whereas $\alpha < 1$ corresponds to a cored profile, and $\alpha > 1$ to a cuspier profile. Under the assumed SHMR and concentration ($c = 5$), we find that low-mass galaxies with high $f_{\rm DM}$ are associated with cuspy distributions, converging towards an NFW-like profile at higher masses with a scatter at least in part driven by their star-formation state. To highlight this, we colour-code the galaxies by the ratio of their SFR averaged over 10 and 100 Myr, $\mathrm{SFR}_{10}/\mathrm{SFR}_{100}$, applying LOESS smoothing (M. Cappellari et al. 2013b). Galaxies going through a burst of star formation ($\log \mathrm{SFR}_{10}/\mathrm{SFR}_{100} \gtrapprox 0.4$) have preferentially high values of α, which supports the adiabatic contraction scenario. This mass dependence differs from the trends observed at $z \sim 0$ from simulations (E. Tollet et al. 2016; J. Freundlich et al. 2020b).

On the other hand, high central baryonic concentrations are expected to perturb the underlying DM distribution and pull the DM towards the centre, increasing the 'cuspiness' of its density profile. This phenomenon is called adiabatic contraction (G. R. Blumenthal et al. 1986), and is represented by the $\alpha > 1$ region of Fig. 6. For galaxies in this region, adiabatic contraction is needed to explain the high $f_{\rm DM}$ values measured in this work. Interestingly, this underprediction of $f_{\rm DM}$, compared to our observations, holds for many other SMHM relations from the literature which typically lie above the P. Behroozi et al. (2019) one (e.g. S. Tacchella et al. 2018). In order to bridge some of the discrepancies between the model predictions and our measurements, a lower SMHM relation at high redshift would be needed. This problem is emphasized by recent predictions from observations and simulations of high DM fractions in low-mass galaxies (A. de Graaff et al. 2024b; W. McClymont et al. 2025c). However, it is important to note that our high $\alpha \gtrapprox 1.5$ values suffer from large uncertainties that make them consistent with $\alpha \approx 1.5$. These stem from the smaller masses of these systems, which make their morphology and kinematics more difficult to constrain.

We colour-code our points in Fig. 6 by their SFHs, parametrized by the ratio of SFR averaged over 10 and 100 Myr. Galaxies with rising SFHs will have positive values of $\mathrm{SFR}_{10}/\mathrm{SFR}_{100}$, whereas galaxies with falling SFHs will show the opposite behaviour. In order to visually assess the presence of an underlying trend, we combine our points in larger bins and use the locally estimated scatterplot smoothing (LOESS) method (M. Cappellari et al. 2013b) to average over single objects and obtain mean estimates for the full sample. We can see a trend of galaxies going through a burst $\log \mathrm{SFR}_{10}/\mathrm{SFR}_{100} \gtrapprox 0.4$ having preferentially higher values of α. This apparent correlation supports the adiabatic contraction scenario that would occur with the inflow of baryons to the central regions during a burst, during which the gas content of the galaxy contracts (A. Dekel & A. Burkert 2014; S. Tacchella et al. 2016b; W. McClymont et al. 2025b). When feedback from the star formation kicks in, driving the gas out of the centre and temporarily quenching star formation, galaxies begin to move back down towards the MS $\log \mathrm{SFR}_{10}/\mathrm{SFR}_{100} < 0$. These galaxies appear to preferentially have cored profiles, consistent with kinetic heating of the DM. This interpretation would imply the interaction of baryons and DM on relatively short time-scales ($t \approx 100$ Myr). However, typical models of core formation suggest that they would form on longer time-scales, comparable to the dynamical time-scales within the galaxy (J. Freundlich et al. 2020a). Studying these time-scales in detail within observations and simulations is a scope for future work. Interestingly, we also find that the values of α correlate with the Sérsic index n measured from the stellar light distribution in the UV (Fig. A1). Galaxies with cuspier DM profiles also have steeper central light profiles, with $n \sim 4$, which could point to interactions between the two components.

We find that low-mass galaxies $\log(M_\star[\mathrm{M}_\odot]) < 9$ have cuspier profiles, while higher mass galaxies seem to converge towards NFW profiles ($\alpha = 1$) with scatter driven by their star-formation state (parametrized by $\mathrm{SFR}_{10}/\mathrm{SFR}_{100}$). This is not necessarily intuitive given the initial discovery of cored systems in dwarf galaxies in the local Universe. However, this can be reconciled when considering burstiness. At high redshift, galaxies have been shown to grow through bursts of star formation (e.g. C.-A. Faucher-Giguère 2018; S. Tacchella, J. C. Forbes & N. Caplar 2020; C. Simmonds et al. 2025; W. McClymont et al. 2025a) at all masses. These bursts are tied to the formation of cores through energetic stellar feedback, smoothing the DM profile in the central regions of galaxies. The more massive galaxies in our sample will have undergone more bursts in their lifetime, leading to a flattening of their DM profiles and resulting in the more

cored profiles we predict in this work. Also, these galaxies could undergo breathing cycles of compaction phases (K. El-Badry et al. 2016; S. Tacchella et al. 2016a). Interestingly, M. Kohandel, A. Pallottini & A. Ferrara (2025) find that one of their most massive galaxies ('Amaryllis', $\log(M_\star[\mathrm{M}_\odot]) = 10.3$ at $z = 7$) has a cored inner DM density profile which reflects the cusp–flattening impact of baryonic feedback. At $z \sim 1$, N. F. Bouché et al. (2022) find that galaxies above the main sequence, and with high SFR surface densities, have preferentially cored DM profiles. This is consistent with star formation influencing the DM profile on relatively short time-scales.

In the local Universe, star formation is smoother, with massive star-forming galaxies growing more smoothly inside out once their central bulges have developed. These massive galaxies undergo long-lived stable growth episodes that could allow their DM profile to stabilise around NFW profiles. On the other hand, dwarf galaxies still have bursty star formation (P. F. Hopkins et al. 2014, 2023; C. C. Hayward & P. F. Hopkins 2017), giving rise to their cores. It is also important to once again consider the evolution of sizes. These dwarf galaxies have larger radii than low-mass galaxies at the same mass in our sample. This naturally implies higher concentrations, which could fuel processes of adiabatic contraction for which we see evidence in Fig. 6.

Finally, we assess how sensitive our results are to the adopted assumptions and discuss their potential impact on our conclusions. Starting with the concentration, changing the value of c affects the distribution of α we find. Specifically, higher concentrations $c > 5$ require more galaxies to have cored profiles $\alpha < 1$ in order to reconcile the predicted fractions f_{DM} with our measured ones. In contrast, lower concentrations, $c < 3$, would have the opposite effect. The most important choice is the SMHM function, which directly affects the normalization of our profiles and, hence, of the α values that we infer. Studies based on simulations and empirical models at high redshift suggest that the normalization of the SMHM relation is higher than the P. Behroozi et al. (2019) one assumed in this work (e.g. see S. Tacchella et al. 2018). This means that the halo mass M_{halo} at fixed stellar mass $M_\star$ is lower than predicted by the P. Behroozi et al. (2019) relation, meaning our profiles would need to be even cuspier (higher α) to reproduce our high f_{DM} values. A last assumption is the choice of profile for the fit, as other profiles such as the Einasto profile (J. Einasto 1965), have also been shown to provide good fits to DM profiles in cosmological simulations (A. A. Dutton & A. V. Macciò 2014). We explored this profile and found no significant change in the observed trends of cuspiness with f_{DM}, $\mathrm{SFR}_{10}/\mathrm{SFR}_{100}$, and $M_\star$. However, our points become more scattered in these parameter spaces. At $z \sim 1$, B. I. Ciocan et al. (2025) showed that the A. Di Cintio et al. (2014) $\alpha\beta\gamma$ parametrization is favoured when fitting the rotation curves in their sample. With this profile, they find that the low-mass galaxies in their sample are predominantly cored, whereas the higher-mass ones show more scatter, with many having cuspier profiles. This trend is consistent with simulation predictions at $z \sim 0$ (e.g. Numerical Investigation of a Hundred Astrophysical Objects (NIHAO); E. Tollet et al. 2016; J. Freundlich et al. 2020b), which are shown in Fig. 6. In this work, we find an opposite trend, as seen in Fig. 6. As discussed above, this could be a redshift effect, since star formation is much more bursty at high redshift, and galaxies are also more compact. Specifically, this compactness could promote adiabatic contraction in low-mass galaxies, which does not occur in their more diffuse counterparts at lower redshift.

None the less, it is essential to note that the choice of profile parametrization may also have a significant impact on the derived inner slope, which could help alleviate this tension. We chose to study the modified NFW profile in the most detail because of the direct comparison it offers with the NFW ($\alpha = 1$) case (equation 18). The inner slope (named s_1) in J. Freundlich et al. (2020b) is defined through the Dekel-Zhao profile (J. Freundlich et al. 2020b), and is computed at 0.01 R_{vir}. This slope corresponds closely to the E. Tollet et al. (2016) slope, which is taken as the average between 0.01 R_{vir} and 0.02 R_{vir}. Within this framework, the NFW slope is $s_1 \approx 1.25$, which differs from the $\alpha = 1$ in our parametrization. None the less, we plot the $s_1 - M_\star$ trend from J. Freundlich et al. (2020b) at $z \approx 0$ (Fig. 6) to offer a qualitative comparison with our measurements of the slope at $z \approx 5$.

Although it is informative to discuss empirical model predictions in the context of our results, it is also important to discuss the caveats of the measurements that could potentially reconcile our inferred profiles with shapes closer to NFW. We discuss these in the next two sections, focusing on the uncertainties in the baryonic and the DM contents.

5.2 Uncertainties in the baryonic content

When calculating baryonic masses needed to infer gas and DM fractions, we need to make some assumptions, of which we will now discuss the implications. First, the stellar mass is inferred using the SED-fitting code PROSPECTOR, a method with many advantages, but also some degeneracies. We attempt to break some of the degeneracies by fixing the redshift to the grism spectroscopic redshift, and by simultaneously fitting the photometry with the line fluxes of the available emission lines (see Section 2). Despite this, we are not fitting spectra and do not have strong constraints for all emission lines, for instance, those constraining nebular metallicities and dust content. Furthermore, our S/N cut implies selecting galaxies whose young stellar population is dominating the SED. This may hamper the detection of the underlying population of older stars, and hence constrain the full SFH. This effect is called 'outshining' and can cause an underestimate of the stellar masses, effectively only attributing the stellar mass to the more visible young stellar population (E. F. Bell & R. S. de Jong 2001; C. Maraston et al. 2010; J. Leja et al. 2019; C. Giménez-Arteaga et al. 2023; S. Tacchella et al. 2023). This would directly affect the measurements of $f_{\mathrm{DM}} < 0$, alleviating the tension by increasing the total baryonic mass.

Uncertainties in the stellar mass and SFRs are propagated into the gas mass estimates derived using the scaling relation by L. J. Tacconi et al. (2018) and L. J. Tacconi et al. (2020). This relation is calibrated out to $z \sim 5.5$, and should hence provide a better estimate of the gas in our galaxies than relations calibrated at much lower redshifts (e.g. J. Kennicutt 1998). None the less, the use of scaling relations does not necessarily encompass the large variety of gas fractions observed at fixed mass (e.g. W. McClymont et al. 2025c), and could introduce biases. Importantly, the L. J. Tacconi et al. (2020) relation is only calibrated above $\log(M_\star[\mathrm{M}_\odot]) \gtrapprox 9$. The extrapolation to the lower masses in our sample results in very high gas fractions $f_{\mathrm{gas}} \sim 1$.

Finally, our adopted scaling relations are only for cold gas, and therefore assume a negligible contribution of the atomic gas. However, recent H I stacking estimates beyond $z \sim 0$ have shown

that this component may not be negligible at higher redshifts (A. Chowdhury et al. 2020; A. Chowdhury, N. Kanekar & J. N. Chengalur 2022a, b; A. Bera et al. 2023; A. Bianchetti et al. 2025). A. Chowdhury et al. 2022a even suggest that the atomic gas dominates the baryonic component at $z \sim 1.3$, the highest redshift at which it is probed. Given the lack of direct constraints on atomic gas at $z > 4$, we are not able to account for it in our calculations of the gas fractions, but if its contribution is significant, this would imply even larger gas fractions than reported here, and therefore lower DM fractions.

5.3 Uncertainties in the DM content

The kinematic measurements, described in A. L. Danhaive et al. (2025b), are the main factor driving the measurement of $f_{\rm DM}$ through their estimate of the dynamical mass. The key assumption made when deriving the dynamical mass is that the measured velocity gradients are tracing rotation of the gas around the galaxy. However, especially at low masses, we cannot rule out the contribution of non-circular motions, typically in the form of outflows (S. Carniani et al. 2024; L. R. Ivey et al. 2025), to our measurement of velocity gradients and dispersions. Such a contribution would bias both quantities to higher values and unphysically boost the inferred dynamical masses, and hence the DM fractions. Also, albeit of smaller importance, the circular velocities needed to compute the dynamical masses are inferred assuming a virialized rotating disc with an exponential light profile. For galaxies with larger Sérsic indices, this assumption can lead to biased results. Furthermore, for pressure-dominated systems, the choice of the pressure support term multiplying the σ_0 in equation (7) can lead to over or underestimates of the circular velocity (see S. H. Price et al. 2022, for detailed analysis).

For the derived relations for both the gas and importantly the DM fractions, we note that we suffer from incompleteness at the low-mass end ($\log(M_\star[{\rm M}_\odot]) < 9$), which could significantly bias our results. In order to obtain meaningful (i.e. resolved) kinematic measurements for low-mass systems, they need to be not only bright in Hα, but also have relatively large rotational velocity and/or velocity dispersions. This could cause our $f_{\rm gas}$ to be biased high (due to the high SFR requirement for the bright Hα) as well as our $f_{\rm DM}$ (due to the high circular velocities). Accounting for these selection effects would move our observed medians closer to the simulations in Fig. 3. Within the paper, we discuss the observed trends, but cannot make definitive conclusions about the behaviour at the low masses. This also translates to incompleteness for galaxies with low baryonic surface densities.

In this discussion, there is a last component that we have not considered, namely the presence of BHs in our galaxies. We investigate this possibility in the next section.

5.4 Overmassive BHs

Although BHs typically represent a small fraction of the total mass, with $M_{\rm BH}/M_\star < 1$ per cent at $z \sim 0$ (A. E. Reines & M. Volonteri 2015), they could have non-negligible effects on the kinematics of their host galaxies through potentially disruptive feedback mechanisms. Furthermore, many recent studies have reported overmassive BHs in the early Universe, with high $M_{\rm BH}/M_\star$ ratios (A. C. Carnall et al. 2023; Y. Harikane et al. 2023; V. Kokorev et al. 2023; H. Übler et al. 2023, 2024; L. J. Furtak et al. 2024; P. Natarajan et al. 2024; R. Maiolino et al. 2024a, b; I. Juodžbalis et al. 2025a) and in some cases even high $M_{\rm BH}/M_{\rm dyn}$ ratios (F. D'Eugenio et al. 2025; X. Ji et al. 2025; I. Juodžbalis et al. 2025b) relative to the local scaling relations.

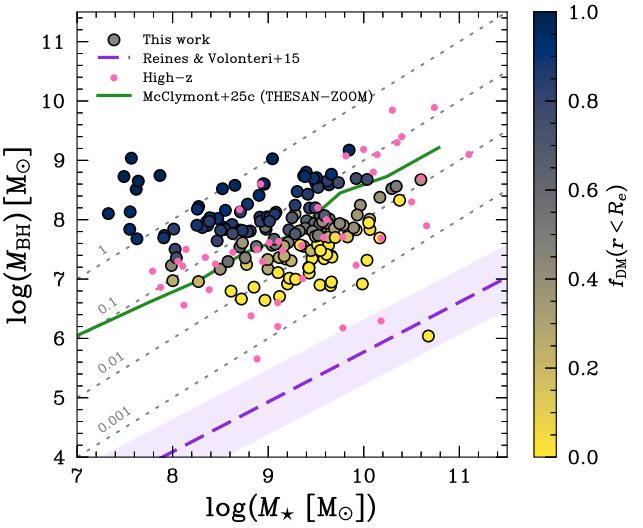

Figure 7. Predicted black hole masses $M_{\rm BH}$, assuming the local $M_{\rm BH} - M_{\rm dyn}$ relation from J. Kormendy & L. C. Ho (2013), as a function of stellar mass (circles). We compare our measurements with the overmassive black holes reported at high redshift ($z \approx 4 - 11$) from *JWST* (pink dots; A. C. Carnall et al. 2023; Y. Harikane et al. 2023; V. Kokorev et al. 2023; H. Übler et al. 2023, 2024; L. J. Furtak et al. 2024; J. E. Greene et al. 2024; I. Juodžbalis et al. 2024; R. Maiolino et al. 2024a, b; J. Matthee et al. 2024; P. Natarajan et al. 2024), which lie well above the local relation (purple dashed line; A. E. Reines & M. Volonteri 2015). The dashed grey lines represent constant ratios of $M_{\rm BH}/M_\star$. We find excellent agreement with the parameter space spanned by these sources, suggesting the shift in the $M_{\rm BH} - M_\star$ relation is consistent with the high gas and DM fractions found in high-redshift galaxies. This is consistent with results from W. McClymont et al. (2025c) following a similar approach to this work but with the THESAN-ZOOM simulations.

Measurements of BH masses are often based on the width of the broadened Balmer lines and contain large uncertainties. We derive estimates of BH masses based solely on the dynamical masses, and assuming the $M_{\rm BH} - M_{\rm dyn}$ relation from J. Kormendy & L. C. Ho (2013), which has been shown to hold at high redshift for most cases (R. Maiolino et al. 2024b; I. Juodžbalis et al. 2025b). These inferred BH masses are not direct measurements. Our goal is to investigate where our sample would lie on the $M_{\rm BH}/ - M_\star$ relation if our galaxies hosted BHs, providing constraints independent of typical BH mass measurements. We show our results in Fig. 7.

We find BH masses spanning a wide range ($\log(M_{\rm BH}[{\rm M}_\odot]) = 6.5 - 9$) and BH-to-stellar mass ratios ($M_{\rm BH}/M_\star = 0.001 - 1$). Interestingly, our sample overlaps with most of the overmassive BHs reported at high redshift. This suggests that, given a fixed $M_{\rm BH} - M_{\rm dyn}$ relation like we have assumed here, these overmassive BHs (relative to the $M_{\rm BH} - M_\star$ plane) are a natural consequence of the high gas and DM fractions found at high redshift (Fig. 4). This is consistent with the results from W. McClymont et al. (2025c), who applied a similar semi-empirical approach to the THESAN-ZOOM simulations, whose model does not include BHs, to predict BH masses in the post-processing. Our results imply that ratios of $M_{\rm BH}/M_\star \approx 0.1$ would be common at high-redshift, and that BHs grow faster at early times, in comparison to the stellar content, than at late times. Because both growth mechanisms require gas inflow, the gas must collapse enough to

accrete on to the BH but without forming many stars. BH growth would need to differ at high redshift in order to reproduce these high $M_{\rm BH}/M_\star$ ratios. However, confirming the presence of BHs at high redshift has proven difficult with our current emission line diagnostics (e.g. G. Mazzolari et al. 2024; L. R. Ivey et al. 2025; J. Scholtz et al. 2025), and various emission line ratios need to be detected spectroscopically, which we do not probe with the grism data used in this work. Also, many models expect that the bulk of the BH population at high-z should be dormant (e.g. R. Schneider et al. 2023; A. Trinca et al. 2024), with short duty cycles for accretion, meaning that we would not expect to see evidence of accreting BHs.

Finally, we discuss the implications of our galaxies hosting BHs. Our findings imply that the BHs could have a significant impact on their host galaxies. Although including their masses in our calculation of $f_{\rm DM}$ does not strongly affect these measurements, due to the small $M_{\rm BH}/M_{\rm dyn}$ values (J. Kormendy & L. C. Ho 2013), accreting BHs could affect the kinematics of the surrounding gas and introduce biases in the measurement of $M_{\rm dyn}$. If present, these AGNs could be categorized as Type II, narrow-line AGNs, and hence would not be detected through the broadening of emission lines caused by the broad-line region. Additionally, AGN-driven outflows in low-mass galaxies would have similar velocities to those measured in this work ($v \sim 100-200$ km s^{-1}; e.g. L. R. Ivey et al. 2025), and could hence boost our measured DM fractions. We note that the lowest mass systems $\log(M_\star[{\rm M}_\odot]) < 8$ in our sample have abnormally high dynamical masses, leading to high predictions of $M_{\rm BH}$, pointing to a likely contribution from non-circular motions, as also shown in Section 3.

6 SUMMARY AND CONCLUSIONS

This work presents the dynamical mass measurements of 163 Hα emitters at $z \approx 4-6$ from the FRESCO and CONGRESS *JWST* grism surveys in the GOODS fields. We model the kinematics of the Hα emission line using forward-modelling and fitting of the grism data with GEKO (A. L. Danhaive & S. Tacchella 2025), recovering in particular rotational velocities and velocity dispersions. Using our measured dynamical masses from our modelling, stellar masses inferred from SED modelling, and gas masses estimated from the L. J. Tacconi et al. (2020) scaling relation, we obtain the gas fractions ($f_{\rm gas}$) and DM fractions ($f_{\rm DM}$) within the Hα half-light radius ($r_{\rm e}$). We summarize our main findings here:

(i) The $\log(M_\star[{\rm M}_\odot]) \approx 7-10$ star-forming galaxies in our sample have relatively high dynamical masses in the range $\log(M_{\rm dyn}[{\rm M}_\odot]) \approx 9-11$. At fixed stellar mass, there is a large scatter in the dynamical masses, indicative of unsettled kinematics. This scatter naturally manifests itself in the Tully–Fisher plane, suggesting that the relation is only beginning to emerge at $z \sim 5$.

(ii) Using gas masses inferred from empirical scaling relations and combined with stellar masses to define baryonic masses, we find that the galaxies in our sample are, on average, gas-rich, with a median inferred gas-to-baryonic mass fraction of $\langle f_{\rm gas}\rangle = 0.77$.

(iii) Based on these baryonic masses and the dynamical mass measurements, we find high central dark-matter fractions within the effective radius, with a median value of $\langle f_{\rm DM}\rangle = 0.73$. Approximately 67 per cent of the galaxies are DM-dominated within $r_{\rm e} \sim 0.5$–1 kpc ($f_{\rm DM} > 0.5$), although the inferred DM fractions span the full range of the parameter space.

(iv) We find evidence for a negative dependence of $f_{\rm DM}$ on stellar mass $M_\star$ as parametrized by equation (14). Specifically, we find $\alpha = 0.28 \pm 0.05$, with low-mass ($\log(M_\star[{\rm M}_\odot]) < 9$) galaxies showing high DM fractions and higher mass galaxies ($\log(M_\star[{\rm M}_\odot]) > 9$) showing a larger diversity, with typically lower $f_{\rm DM}$.

(v) We find an anticorrelation ($\rho = -0.56$, $p < 0.001$) between $f_{\rm DM}$ and the baryonic surface density $\Sigma_{\rm bar}$ within $r_{\rm e}$, consistent with but weaker than its counterpart at cosmic noon and the local Universe. The galaxies in our sample have high baryonic surface densities comparable to those of more massive galaxies at cosmic noon, caused by their compactness and high central gas fractions.

(vi) Our high DM fractions are consistent with the predicted progenitor populations of $z \sim 2$ baryon-dominated systems, as shown by a comparison with the TNG50 and THESAN-ZOOM simulations. These high fractions are expected for low-mass galaxies at all redshifts.

(vii) Assuming a modified NFW profile, a stellar-to-halo mass function, and a DM profile concentration, we qualitatively explore the predicted shape of the underlying DM halo density profile for our sample. We find that the higher-mass, baryon-dominated systems would need a cored profile to reconcile their low fractions. This core could have been induced by repeated bursts of star formation. In contrast, the low-mass, high $f_{\rm DM}$ systems are consistent with cuspier DM profiles, suggesting adiabatic contraction pulling more DM into the central regions.

(viii) Finally, we find that our elevated $f_{\rm gas}$ and $f_{\rm DM}$ naturally anticipate the population of overmassive BHs found with *JWST* at high-redshift, when assuming a $M_{\rm BH} - M_{\rm dyn}$ relation.

Our study extends, for the first time, measurements of DM fractions to large statistical samples at high redshift, advancing beyond previous analyses focused on ionized-gas kinematics at cosmic noon. Although our inferences rely on several necessary assumptions, they provide a valuable framework for placing spatially resolved measurements of individual systems into a broader population context. Most importantly, this work establishes a foundation for probing DM haloes through high-redshift observations, which is an essential step towards understanding how baryons and dark matter interact and co-evolve during the early stages of galaxy formation.

ACKNOWLEDGEMENTS

We thank the referee for the insightful comments that improved the paper. We thank Hannah Übler and Andreas Burkert for the insightful discussions. ALD thanks the University of Cambridge Harding Distinguished Postgraduate Scholars Programme and Technology Facilities Council (STFC) Center for Doctoral Training (CDT) in Data intensive science at the University of Cambridge (STFC grant number 2742605) for a PhD studentship. ALD and ST acknowledge support by the Royal Society Research Grant G125142. AJB acknowledges funding from the 'FirstGalaxies' Advanced Grant from the European Research Council (ERC) under the European Union's Horizon 2020 research and innovation programme (Grant agreement No. 789056). ECL acknowledges support of an STFC Webb Fellowship (ST/W001438/1). FDE and RM acknowledge support by the Science and Technology Facilities Council (STFC), by the ERC through Advanced Grant 695671 'QUENCH', and by the UKRI Frontier Research grant RISEandFALL. EE, BDJ, MR, CNAW, and YZ are sup-

ported by the *JWST*/NIRCam contract to the University of Arizona, NAS5-02105. DJE was supported as a Simons Investigator and by *JWST*/NIRCam contract to the University of Arizona, NAS5-02105. Support for program #3215 was provided by NASA through a grant from the Space Telescope Science Institute, which is operated by the Association of Universities for Research in Astronomy, Inc., under NASA contract NAS 5-03127. WM thanks the Science and Technology Facilities Council (STFC) Center for Doctoral Training (CDT) in Data Intensive Science at the University of Cambridge (STFC grant number 2742968) for a PhD studentship. BER acknowledges support from the NIRCam Science Team contract to the University of Arizona, NAS5-02105, and JWST Program 3215.

This work is based on observations made with the NASA/ESA *Hubble Space Telescope* and NASA/ESA/CSA *James Webb Space Telescope*. The data were obtained from the Mikulski Archive for Space Telescopes at the Space Telescope Science Institute, which is operated by the Association of Universities for Research in Astronomy, Inc., under NASA contract NAS 5-03127 for *JWST*. These observations are associated with program #1180, 1181, 1210 (JADES), #1895 (FRESCO), # 1963 (JEMS), and #3577 (CONGRESS). Support for program #3577 was provided by NASA through a grant from the Space Telescope Science Institute, which is operated by the Association of Universities for Research in Astronomy, Inc., under NASA contract NAS 5-03127. The authors acknowledge the FRESCO team for developing their observing programme with a zero-exclusive-access period. The authors acknowledge use of the lux supercomputer at UC Santa Cruz, funded by NSF MRI grant AST 1828315.

DATA AVAILABILITY

The data underlying this article will be shared on reasonable request to the corresponding author. Fully reduced NIRCam images are publicly available on MAST (https://archive.stsci.edu/hlsp/jades), with doi:10.17909/8tdj-8n28, doi:10.17909/z2gwmk31, and doi:10.17909/fsc4-dt61 (D. J. Eisenstein et al. 2023; M. J. Rieke et al. 2023). The NIRCam grism spectra are publicly available on MAST with doi:10.17909/6rfk-6s81 and doi:0.17909/gdyc-7g80 (P. A. Oesch et al. 2023).

REFERENCES

Allen N. et al., 2025, A&A, 698, A30
Barnabè M. et al., 2012, MNRAS, 423, 1073
Behroozi P., Wechsler R. H., Hearin A. P., Conroy C., 2019, MNRAS, 488, 3143
Behroozi P. S., Conroy C., Wechsler R. H., 2010, ApJ, 717, 379
Bell E. F., de Jong R. S., 2001, ApJ, 550, 212
Bera A., Kanekar N., Chengalur J. N., Bagla J. S., 2023, ApJ, 950, L18
Bianchetti A. et al., 2025, ApJ, 982, 82
Blumenthal G. R., Faber S. M., Flores R., Primack J. R., 1986, ApJ, 301, 27
Bouché N. F. et al., 2022, A&A, 658, A76
Brammer G. B., van Dokkum P. G., Coppi P., 2008, ApJ, 686, 1503
Bullock J. S., Boylan-Kolchin M., 2017, ARA&A, 55, 343
Burkert A., 1995, ApJ, 447, L25
Burkert A., Silk J., 1997, ApJ, 488, L55
Burkert A. et al., 2010, ApJ, 725, 2324
Calabrese E., Spergel D. N., 2016, MNRAS, 460, 4397
Cappellari M. et al., 2013a, MNRAS, 432, 1709
Cappellari M. et al., 2013b, MNRAS, 432, 1862
Carnall A. C. et al., 2023, Nature, 619, 716
Carniani S. et al., 2024, A&A, 685, A99
Ceverino D., Glover S. C. O., Klessen R. S., 2017, MNRAS, 470, 2791
Chan T. K., Kereš D., Oñorbe J., Hopkins P. F., Muratov A. L., Faucher-Giguère C. A., Quataert E., 2015, MNRAS, 454, 2981
Chowdhury A., Kanekar N., Chengalur J. N., Sethi S., Dwarakanath K. S., 2020, Nature, 586, 369
Chowdhury A., Kanekar N., Chengalur J. N., 2022a, ApJ, 935, L5
Chowdhury A., Kanekar N., Chengalur J. N., 2022b, ApJ, 941, L6
Ciocan B. I., Bouché N. F., Fensch J., Mercier W., Krajnović D., Richard J., Contini T., Jeanneau A., 2025, preprint (arXiv:2506.19721)
Conroy C., Wechsler R. H., Kravtsov A. V., 2006, ApJ, 647, 201
Cooray A., Sheth R., 2002, Phys. Rep., 372, 1
Courteau S., 1997, AJ, 114, 2402
Covelo-Paz A. et al., 2025, A&A, 694, A178
Covington M. D. et al., 2010, ApJ, 710, 279
Cresci G. et al., 2009, ApJ, 697, 115
D'Eugenio C. et al., 2021, A&A, 653, A32
D'Eugenio F. et al., 2025, preprint (arXiv:2503.11752)
Dalcanton J. J., Stilp A. M., 2010, ApJ, 721, 547
Danhaive A. L., Tacchella S., 2025, preprint (arXiv:2510.07369)
Danhaive A. L. et al., 2025a, preprint (arXiv:2510.06315)
Danhaive A. L. et al., 2025b, MNRAS, 543, 3249
de Blok W. J. G., 2010, Adv. Astron., 2010, 789293
de Graaff A. et al., 2024a, A&A, 684, A87
de Graaff A., Pillepich A., Rix H.-W., 2024b, ApJ, 967, L40
Dekel A., Burkert A., 2014, MNRAS, 438, 1870
Dekel A. et al., 2021, MNRAS, 508, 999
Di Cintio A., Brook C. B., Dutton A. A., Macciò A. V., Stinson G. S., Knebe A., 2014, MNRAS, 441, 2986
Dutton A. A., Macciò A. V., 2014, MNRAS, 441, 3359
Einasto J., 1965, Trudy Astrofizicheskogo Instituta Alma-Ata, 5, 87
Eisenstein D. J. et al., 2023, preprint (arXiv:2306.02465)
El-Badry K., Wetzel A., Geha M., Hopkins P. F., Kereš D., Chan T. K., Faucher-Giguère C.-A., 2016, ApJ, 820, 131
El-Zant A. A., Freundlich J., Combes F., 2016, MNRAS, 461, 1745
Faucher-Giguère C.-A., 2018, MNRAS, 473, 3717
Foreman-Mackey D., Hogg D. W., Lang D., Goodman J., 2013, PASP, 125, 306
Freundlich J. et al., 2019, A&A, 622, A105
Freundlich J., Dekel A., Jiang F., Ishai G., Cornuault N., Lapiner S., Dutton A. A., Macciò A. V., 2020a, MNRAS, 491, 4523
Freundlich J. et al., 2020b, MNRAS, 499, 2912
Furtak L. J. et al., 2024, Nature, 628, 57
Genzel R. et al., 2015, ApJ, 800, 20
Genzel R. et al., 2017, Nature, 543, 397
Genzel R. et al., 2020, ApJ, 902, 98
Giménez-Arteaga C. et al., 2023, ApJ, 948, 126
Girelli G., Pozzetti L., Bolzonella M., Giocoli C., Marulli F., Baldi M., 2020, A&A, 634, A135
Gnedin O. Y., Kravtsov A. V., Klypin A. A., Nagai D., 2004, ApJ, 616, 16
Goodman J., Weare J., 2010, Commun. Appl. Math. Comput. Sci., 5, 65
Greene J. E. et al., 2024, ApJ, 964, 39
Hainline K. N. et al., 2024, ApJ, 964, 71
Harikane Y. et al., 2023, ApJ, 959, 39
Hayward C. C., Hopkins P. F., 2017, MNRAS, 465, 1682
Helton J. M. et al., 2024, ApJ, 974, 41
Hopkins P. F., Kereš D., Oñorbe J., Faucher-Giguère C.-A., Quataert E., Murray N., Bullock J. S., 2014, MNRAS, 445, 581
Hopkins P. F. et al., 2023, MNRAS, 525, 2241
Hu W., Barkana R., Gruzinov A., 2000, Phys. Rev. Lett., 85, 1158
Ivey L. R. et al., 2026, preprint (arXiv:2507.14936)
Ji X. et al., 2025, MNRAS, 544, 3900
Ji Z. et al., 2024, preprint (arXiv:2401.00934)
Johnson B. D., Leja J., Conroy C., Speagle J. S., 2021, ApJS, 254, 22
Jones B. L. et al., 2025, preprint (arXiv:2510.07376)
Jones O. C. et al., 2023, MNRAS, 523, 2519

Juodžbalis I. et al., 2024, Nature, 636, 594
Juodžbalis I. et al., 2025a, preprint (arXiv:2504.03551)
Juodžbalis I. et al., 2025b, preprint (arXiv:2508.21748)
Kannan R. et al., 2025, The Open Journal of Astrophysics, 8, 153
Kashino D., Lilly S. J., Matthee J., Eilers A.-C., Mackenzie R., Bordoloi R., Simcoe R. A., 2023, ApJ, 950, 66
Kennicutt Robert C. J., 1998, ARA&A, 36, 189
Kennicutt R. C., Evans N. J., 2012, ARA&A, 50, 531
Kohandel M., Pallottini A., Ferrara A., 2025, A&A , 704, A39
Kokorev V. et al., 2023, ApJ, 957, L7
Kormendy J., Ho L. C., 2013, ARA&A, 51, 511
Koudmani S., Henden N. A., Sijacki D., 2021, MNRAS, 503, 3568
Koudmani S., Sijacki D., Smith M. C., 2022, MNRAS, 516, 2112
Kravtsov A. V., Berlind A. A., Wechsler R. H., Klypin A. A., Gottlöber S., Allgood B., Primack J. R., 2004, ApJ, 609, 35
Kravtsov A. V., Vikhlinin A. A., Meshcheryakov A. V., 2018, Astron. Lett., 44, 8
Lee L. L. et al., 2025, A&A, 701, A260
Leja J. et al., 2019, ApJ, 877, 140
Lelli F., McGaugh S. S., Schombert J. M., 2016, ApJ, 816, L14
Lelli F., Di Teodoro E. M., Fraternali F., Man A. W. S., Zhang Z.-Y., De Breuck C., Davis T. A., Maiolino R., 2021, Science, 371, 713
Leroy A. K., Walter F., Brinks E., Bigiel F., de Blok W. J. G., Madore B., Thornley M. D., 2008, AJ, 136, 2782
Li P., McGaugh S. S., Lelli F., Schombert J. M., Pawlowski M. S., 2022, A&A, 665, A143
Li Z., Dekel A., Mandelker N., Freundlich J., François T. L., 2023, MNRAS, 518, 5356
Lin X. et al., 2026, ApJ, 997, 207
Ma X. et al., 2018, MNRAS, 477, 219
Madau P., Dickinson M., 2014, ARA&A, 52, 415
Maiolino R. et al., 2024a, Nature, 627, 59
Maiolino R. et al., 2024b, A&A, 691, A145
Maraston C., Pforr J., Renzini A., Daddi E., Dickinson M., Cimatti A., Tonini C., 2010, MNRAS, 407, 830
Marinoni C., Hudson M. J., 2002, ApJ, 569, 101
Martinsson T. P. K., Verheijen M. A. W., Westfall K. B., Bershady M. A., Andersen D. R., Swaters R. A., 2013, A&A, 557, A131
Martizzi D., Teyssier R., Moore B., 2013, MNRAS, 432, 1947
Matthee J. et al., 2024, ApJ, 963, 129
Mazzolari G. et al., 2024, A&A, 691, A345
McClymont W. et al., 2025a, MNRAS, 544, 1732
McClymont W. et al., 2025b, MNRAS, 544, 1732
McClymont W. et al., 2025c, MNRAS, 545, staf2092
McGaugh S. S., 2005, ApJ, 632, 859
McGaugh S. S., 2012, AJ, 143, 40
McGaugh S. S., Schombert J. M., Bothun G. D., de Blok W. J. G., 2000, ApJ, 533, L99
McMillan P. J., 2017, MNRAS, 465, 76
Milgrom M., 1983, ApJ, 270, 384
Miller S. H., Bundy K., Sullivan M., Ellis R. S., Treu T., 2011, ApJ, 741, 115
Moore B., 1994, Nature, 370, 629
Moster B. P., Somerville R. S., Maulbetsch C., van den Bosch F. C., Macciò A. V., Naab T., Oser L., 2010, ApJ, 710, 903
Natarajan P., Pacucci F., Ricarte A., Bogdán Á., Goulding A. D., Cappelluti N., 2024, ApJ, 960, L1
Navarro J. F., Frenk C. S., White S. D. M., 1997, ApJ, 490, 493
Nelson D. et al., 2019, MNRAS, 490, 3234
Nelson E. J. et al., 2016, ApJ, 828, 27
Nestor Shachar A. et al., 2023, ApJ, 944, 78
Newman S. F. et al., 2013, ApJ, 767, 104
Noordermeer E., van der Hulst J. M., Sancisi R., Swaters R. S., van Albada T. S., 2007, MNRAS, 376, 1513
Oesch P. A. et al., 2023, MNRAS, 525, 2864
Paquereau L. et al., 2025, A&A, 702, A163
Pasha I., Miller T. B., 2023, J. Open Source Softw., 8, 5703
Peacock J. A., Smith R. E., 2000, MNRAS, 318, 1144
Persic M., Salucci P., Stel F., 1996, MNRAS, 281, 27
Phillips S., Rizzo F., Kohandel M., Smit R., Pallottini A., 2025, MNRAS, 544, 2758
Pillepich A. et al., 2019, MNRAS, 490, 3196
Planck Collaboration VI, 2020, A&A, 641, A6
Pontzen A., Governato F., 2012, MNRAS, 421, 3464
Pontzen A., Governato F., 2014, Nature, 506, 171
Pope A. et al., 2023, ApJ, 951, L46
Posti L., Fraternali F., Di Teodoro E. M., Pezzulli G., 2018, A&A, 612, L6
Price S. H. et al., 2016, ApJ, 819, 80
Price S. H. et al., 2020, ApJ, 894, 91
Price S. H. et al., 2022, A&A, 665, A159
Read J. I., Gilmore G., 2005, MNRAS, 356, 107
Read J. I., Agertz O., Collins M. L. M., 2016, MNRAS, 459, 2573
Reines A. E., Volonteri M., 2015, ApJ, 813, 82
Reyes R., Mandelbaum R., Gunn J. E., Pizagno J., Lackner C. N., 2011, MNRAS, 417, 2347
Rieke M. J. et al., 2023, ApJS, 269, 16
Ristea A., Cortese L., Groves B., Fraser-McKelvie A., Obreschkow D., Glazebrook K., 2024, MNRAS, 534, 995
Rizzo F., Vegetti S., Powell D., Fraternali F., McKean J. P., Stacey H. R., White S. D. M., 2020, Nature, 584, 201
Rizzo F., Vegetti S., Fraternali F., Stacey H. R., Powell D., 2021, MNRAS, 507, 3952
Robertson B. et al., 2024, ApJ, 970, 31
Rodríguez-Puebla A., Primack J. R., Avila-Reese V., Faber S. M., 2017, MNRAS, 470, 651
Roman-Oliveira F., Fraternali F., Rizzo F., 2023, MNRAS, 521, 1045
Romeo A. B., Agertz O., Renaud F., 2020, MNRAS, 499, 5656
Rowland L. E. et al., 2024, MNRAS, 535, 2068
Rubin V. C., Ford W. K., Jr., Thonnard N., 1980, ApJ, 238, 471
Rubin V. C., Burstein D., Ford W. K., Jr., Thonnard N., 1985, ApJ, 289, 81
Saintonge A. et al., 2017, ApJS, 233, 22
Saldana-Lopez A. et al., 2025, MNRAS, 544, 132
Schneider R., Valiante R., Trinca A., Graziani L., Volonteri M., Maiolino R., 2023, MNRAS, 526, 3250
Scholtz J. et al., 2025, A&A, 697, A175
Serra P., Oosterloo T., Cappellari M., den Heijer M., Józsa G. I. G., 2016, MNRAS, 460, 1382
Sersic J. L., 1968, Atlas de Galaxias Australes
Sharma G., Salucci P., van de Ven G., 2021, A&A, 653, A20
Sharma G., van de Ven G., Salucci P., Martorano M., 2025, A&A, 699, A164
Shibuya T., Ouchi M., Harikane Y., 2015, ApJS, 219, 15
Shuntov M. et al., 2022, A&A, 664, A61
Shuntov M. et al., 2025, A&A, 695, A20
Sijacki D., Springel V., Di Matteo T., Hernquist L., 2007, MNRAS, 380, 877
Simmonds C. et al., 2024, MNRAS, 535, 2998
Simmonds C. et al., 2025, MNRAS, 544, 4551
Simons R. C. et al., 2016, ApJ, 830, 14
Smith R. E. et al., 2003, MNRAS, 341, 1311
Sonnenfeld A., Treu T., Gavazzi R., Marshall P. J., Auger M. W., Suyu S. H., Koopmans L. V. E., Bolton A. S., 2012, ApJ, 752, 163
Speagle J. S., Steinhardt C. L., Capak P. L., Silverman J. D., 2014, ApJS, 214, 15
Spergel D. N., Steinhardt P. J., 2000, Phys. Rev. Lett., 84, 3760
Sun F. et al., 2023, ApJ, 953, 53
Tacchella S., Dekel A., Carollo C. M., Ceverino D., DeGraf C., Lapiner S., Mandelker N., Primack Joel R., 2016a, MNRAS, 457, 2790
Tacchella S., Dekel A., Carollo C. M., Ceverino D., DeGraf C., Lapiner S., Mandelker N., Primack J. R., 2016b, MNRAS, 458, 242
Tacchella S., Bose S., Conroy C., Eisenstein D. J., Johnson B. D., 2018, ApJ, 868, 92
Tacchella S., Forbes J. C., Caplar N., 2020, MNRAS, 497, 698
Tacchella S. et al., 2023, MNRAS, 522, 6236
Tacconi L. J. et al., 2018, ApJ, 853, 179
Tacconi L. J., Genzel R., Sternberg A., 2020, ARA&A, 58, 157

Tasitsiomi A., 2007, in Axebides M., Fanourakis G., Vergados J., eds, The Identification of Dark Matter. p. 596
Tiley A. L. et al., 2016, MNRAS, 460, 103
Tollet E. et al., 2016, MNRAS, 456, 3542
Trinca A. et al., 2024, preprint (arXiv:2412.14248)
Tully R. B., Fisher J. R., 1977, A&A, 54, 661
Turner O. J. et al., 2017, MNRAS, 471, 1280
Übler H. et al., 2017, ApJ, 842, 121
Übler H. et al., 2021, MNRAS, 500, 4597
Übler H. et al., 2023, A&A, 677, A145
Übler H. et al., 2024, MNRAS, 533, 4287
Vale A., Ostriker J. P., 2006, MNRAS, 371, 1173
van Houdt J. et al., 2021, ApJ, 923, 11
Wang Y. et al., 2020, MNRAS, 491, 5188
Ward E. et al., 2024, ApJ, 962, 176
Wechsler R. H., Tinker J. L., 2018, ARA&A, 56, 435
Weijmans A.-M., Krajnović D., van de Ven G., Oosterloo T. A., Morganti R., de Zeeuw P. T., 2008, MNRAS, 383, 1343
Williams C. C. et al., 2023, ApJS, 268, 64
Wuyts S. et al., 2016, ApJ, 831, 149
Yang L. et al., 2025, ApJS, 281, 68
Zhu K., Lu S., Cappellari M., Li R., Mao S., Gao L., Ge J., 2024, MNRAS, 527, 706
Zhu Y. et al., 2023, MNRAS, 519, 4479

APPENDIX A: SUPPLEMENTARY FIGURES

In Fig. A1, we present additional diagnostic plots that complement the main analysis. This figure illustrates the relation between the inferred inner DM slope α and the DM fraction $f_{\rm DM}$, colour-coded by stellar mass and Sérsic index. The trends shown here are consistent with those discussed in Section 5, reinforcing that galaxies with lower $f_{\rm DM}$ tend to exhibit shallower inner density slopes, while systems with higher $f_{\rm DM}$ favour cuspier profiles. Although the scatter is substantial, these correlations support the interpretation that the interplay between baryonic concentration and halo response is already shaping the inner DM structure at $z \sim 5$.

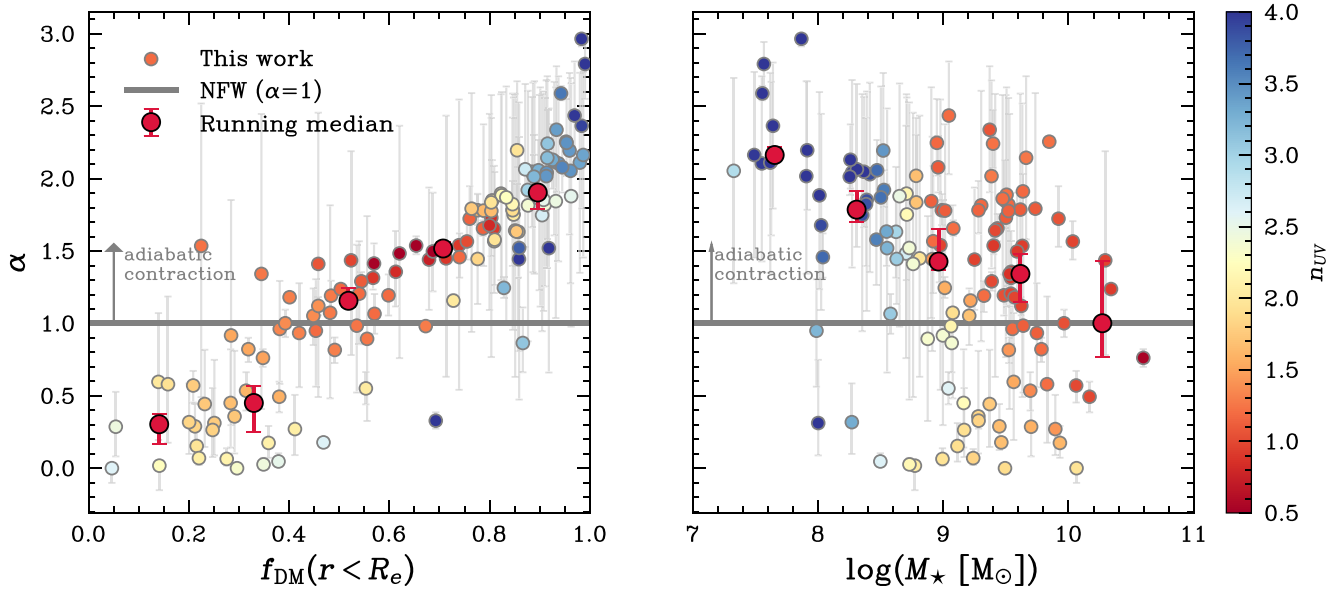

Figure A1. Estimatedslope α of the inner DM density profile for a modified NFW distribution (equation 18) as a function of measured DM fractions (left) and stellar mass (right). A value of $\alpha = 1$ represents the classical NFW profile, whereas $\alpha < 1$ corresponds to a cored profile, and $\alpha > 1$ to a cuspier profile. We find that galaxies with seemingly steeper DM profiles ($\alpha > 1$) coincide with steeper light distributions ($n > 1$) as probed by the UV stellar continuum. To highlight this, we colour-code the galaxies by the Sérsic index $n_{\rm UV}$, applying LOESS smoothing (M. Cappellari et al. 2013b).

This paper has been typeset from a TEX/LATEX file prepared by the author.